buildings

MDPI

Article

Stress Concentration Factors of Concrete-Filled Double-Skin Tubular K-Joints

Qian Xia [1], Ling Ma [2,3], Gang Li [2,3], Chao Hu [1], Lei Zhang [4,*], Fei Xu [4] and Zhenhai Liu [2,3]

[1] Central Southern China Electric Power Design Institute Co., Ltd., Wuhan 430071, China
[2] China Power Engineering Consulting Group Co., Ltd., Beijing 100120, China
[3] Ocean Energy Engineering Technology Research Institute of CPECC, Guangzhou 511400, China
[4] School of Civil Engineering, Chongqing University, Chongqing 400030, China
* Correspondence: leizhang_cqu@163.com

Abstract: Tubular joints are important connecting parts of a welded steel tube structure. The S-N curves based on the hot spot stress (HSS) method are often used to evaluate the fatigue life of tubular joints in practical engineering. The stress concentration factor (SCF) is a key parameter to calculate HSS. In this paper, stress concentration tests of hollow-section and concrete-filled double-skin tubular (CFDST) K-joints were carried out, respectively, and then finite element models of K-joints considering the weld were established. The developed models were validated with the experimental results. The influence of key geometrical parameters, such as the diameter ratio of brace to chord β, the diameter to thickness ratio of chord γ, the wall thickness ratio of brace to chord τ, brace angle θ, and hollow section ratio ζ on the distribution and key position of SCFs along the weld toe, was discussed. Parametric studies were conducted to obtain the calculating equations for the SCF values of CFDST K-joints. The results demonstrate that infill concrete can effectively reduce SCFs along the weld on the chord. When the hollow section ratio was reduced to 0.317, the SCF was reduced by 77.2%. Notably, the SCF reduction rate was sensitive to γ and θ, with a decrease observed as γ increased. The hollow section ratio ζ had a less pronounced effect on SCF distribution patterns, but as ζ decreased, the chord's stiffness improved, suggesting a potential approach to enhance joint performance. The distribution of SCFs is similar for joints of the same type but different geometric configurations. The innovatively integrated hollow section ratio in the CFDST design equation significantly simplifies and enhances the precision of SCF calculations for CFDST K-joints.

Keywords: CFDST; finite element analysis; K-joint; parametric analysis; parametric equation; hot spot stress concentration factor

Citation: Xia, Q.; Ma, L.; Li, G.; Hu, C.; Zhang, L.; Xu, F.; Liu, Z. Stress Concentration Factors of Concrete-Filled Double-Skin Tubular K-Joints. *Buildings* **2024**, *14*, 1363. https://doi.org/10.3390/buildings14051363

Academic Editor: Dan Bompa

Received: 12 April 2024
Revised: 3 May 2024
Accepted: 7 May 2024
Published: 10 May 2024

1. Introduction

In recent years, renewable energy has become increasingly important for addressing global climate change, resource depletion, and environmental degradation. Countries around the world are developing sustainable and renewable energy [1,2]. Several buildings and infrastructures were constructed to include sustainable practices. Several architectural works, such as conventional and public buildings, have used sustainable practices during the design process [3,4], whereas specific studies have concentrated on sustainable practices during the structural design [3,5,6]. Offshore wind energy infrastructure prioritizes sustainability and maximum efficiency based on this study. Offshore wind energy has a clean energy source with the highest efficiency and the greatest potential. Compared with onshore wind energy, offshore wind energy provides better wind conditions and satisfaction of electricity demand, and has garnered increasing attention in recent years [7]. Many wind farms have been developed and constructed on a large scale [8]. Different support structure have been designed for offshore wind turbines in different water depths and environmental conditions [9,10]. Data show that jackets are more cost-effective than

fixed wind turbine foundations in offshore areas, and are the most important support structure of offshore platforms [11]. The jacket foundation of offshore wind platforms is a space truss structure composed of steel pipe components evolved from the technology from offshore oil and gas platforms. With the wide range of installed water depths, higher carrying capacity, and less material consumption, the jacket foundation is regarded as a good choice for an intermediate water depth ranging from 30 to 80 m [7]. However, with the development of offshore wind power, the installed capacity increases, which puts forward higher requirements for the performance of the offshore foundation.

Welded steel tubular joints, serving as the sensitive areas of the jacket structure, are subjected to a complex stress state due to the intersection of weld seams. Under loadings, welded steel tubular joints are constantly subjected to the combined effects of periodic alternating loads, such as wind, waves, currents, and tides, easily leading to microcracks and defect propagation at welding intersection areas, and eventually resulting in bearing capacity degradation and fatigue failure, affecting the safety and stability of the jacket structure. Therefore, the fatigue assessment and life prediction of welded tubular joints in offshore jacket platforms have been attracting increasing attention among scholars in recent years. These experimental and numerical methods aim to provide a more accurate and reliable predictive tool for a standardized design method. Huang et al. conducted experiments and analyzed the failure model and structural behavior of CHS and CFST truss girders. Song et al. [12] conducted experimental and numerical investigations on the mechanical behavior and design method of K and KK CHS joints. Xu et al. investigated the SCF reduction coefficients of CFRP strengthened CHS gap K-joints via a numerical analysis [13], concluding that the CFRP strengthening on the chord and brace had a negligible effect on the stress concentration factor reduction coefficients of circular hollow section gap K-joints. To provide a reliable prediction of the structural behavior of weld tubular joints, CFST K-joints with steel studs were proposed by Ferrotto et al. [14]. Conducing a comprehensive discussion of key parameters using the FE method, according to the high-time computational costs required by actual complex FE models keeping the same accuracy, for CFST K-joints with studs, it was found that it was possible to ploy cohesive interaction properties using contact stiffness coefficients for normal and tangential directions to reproduce the contribution provided by the studs in the overall response of the joint. During the early structural design and service life of tubular joints, the S-N curve method based on hot spot stress is commonly utilized to assess their fatigue life [15]. Hot spot stress is defined as the maximum structural stress at the weld toe, influenced by the overall geometric shape and loading conditions of the welded structure, excluding local stress concentration caused by weld dimensions and defects. The ratio of hot spot stress to nominal stress is defined by the stress concentration factor (SCF). In the hot spot stress-based fatigue design for tubular joints, concentration factors are essential [12,16]. The S-N based on hot spot stress has become a reliable, commonplace method for the fatigue assessment of weld tubular joints, adopted as design principles by the Institute of International Institute of Welding (IIW) [17], Eurocode3 (EN 1993-1-9:2005) [18], the International Committee for Research and Technical Support for Hollow Section Structures (CIDECT), and Det Norske Veritas (DNV, DNV-RP-C203) [19]. The SCF is the key parameter to determine the stress amplitude and perform fatigue analyses [20]. The CIDECT specification [18] and DNV rules [19] have employed the hot spot stress method to assess the S-N curves of circular steel tubular joints with different thicknesses. As the thickness of steel tubes increases, the external load required to achieve the same hot spot stress also rises, resulting in a decrease in the fatigue life of joints under the same hot spot stress. To address these issues, experimental and numerical studies have been conducted domestically and internationally on the stress concentration factors (SCFs) of hollow and concrete-filled steel tubular joints [21–23]. Large-scale concrete-filled K and KK connections were tested, based on experimental stress concentration factor values of both K and KK joints; were compared with predictive results calculated based on design specifications, besides the revised punching shear strength design equation; and were proposed with a reasonable

accuracy [12]. Xu et al. [16] conducted eight full-scale CFST specimen tests and a finite-element analysis on the stress concentration coefficient (SCF). Considering the influence of core concrete on chord deformation mechanics, the releasing coefficient was proposed. The calculation method of SCF for CFST K-joints based on the releasing method of the ST K-joint SCF was established [15]. Based on the modified equivalent thickness, extending the SCF calculation of circular hollow-section joints, a calculation method of SCFs for CFST T/Y joints was proposed by Xiao et al. [20]. These studies have demonstrated that internal core concrete significantly reduces SCFs in concrete-filled steel tubular joints, with values notably lower than those of hollow steel tubular joints. The existing research on the fatigue performance of concrete-filled double-skin tubular (CFDST) K-joints, with a particular emphasis on stress concentration factors (SCFs), is notably deficient. A comprehensive review of the literature has identified an absence of parametric models that directly account for the hollow section ratio in CFDST K-joints. This study aims to fill this knowledge gap through a synergistic approach of experimental investigations and a finite element analysis, thereby contributing to the understanding of SCFs in CFDST K-joints.

In this study, stress concentration tests were conducted on two CHS and three CFDST K-joints, respectively. A detailed finite element model, incorporating the intersecting welds of the brace and chord, was developed. The accuracy of this model was validated by comparing its results with those obtained from experiments, literature-based experiments, and regulatory calculations. Based on the finite element analysis, the distribution pattern of SCFs was determined, and the influence of various geometric parameters on SCFs at critical locations was discussed. Furthermore, 360 finite element models of CHS and CFDST K-joints with different geometric parameters were established. A regression analysis was used to derive parametric formulas for SCFs at critical locations in both types of joints.

2. Materials and Methods

2.1. Specimens

Two CHS K-joints and three CFDST K-joints were fabricated using Q355 steel and C50 self-compacting mortar concrete. Brace members were constructed using seamless hot-rolled steel tubes, while chord members were fabricated from welded steel tubes. To minimize the influence of welds on test outcomes, the weld of chord members were oriented away from the points of attachment where brace members were connected. Full-penetration welds were connected using the Gas-Metal Arc Welding (GMAW) method [24]. Detailed dimensions of the tested CHS and CFDST K-joints are given in Figure 1 and Table 1. The hollow section ratio ζ can be calculated using Equation (1). The dimensions L and l were selected as 1800 and 697 mm for convenience of the installation of the specimens and loading device. The diameter D of the chord was 300 mm for all K-joints. All specimens were labelled as OC300-6-IC203-8-BR121-8, where OC, IC, and BR refer to the outer chord, inner chord, and brace. The numbers following OC, IC, and BR represent the tube diameter (i.e., 300 mm for the outer chord, 203 mm for inner chord, and 121 mm for the brace) and thickness of the corresponding tubes (i.e., 6 mm for the outer chord, 8 mm for the inner chord, and 8 mm for the brace). For CHS K-joints, the inner chord diameter and inner chord thickness are equal to zero. The dimensionless parameters of α, β, γ, τ, and ζ were changed by changing the parameters of T, d, t, D_1, and T_1.

$$\zeta = \frac{D_{\mathrm{i}}}{(D - 2T)} \tag{1}$$

where ζ is the hollow section ratio of the chord for CFDST K-joints, D_1 is the diameter of the inner chord for CFDST K-joints, D is the diameter and thickness of the outer chord for CFDST K-joints, and T is the thickness of the outer chord for CFDST K-joints.

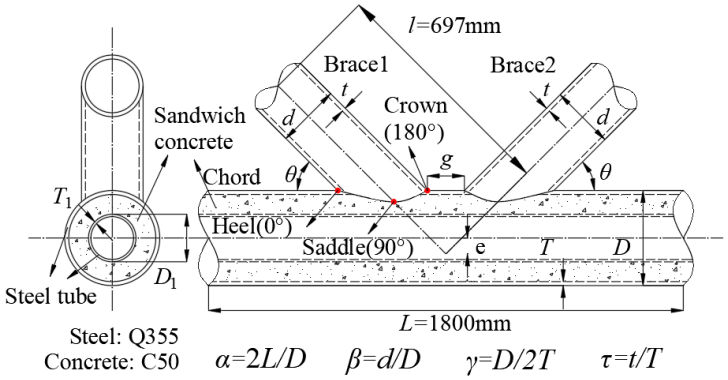

Figure 1. Schematic diagram dimensions of the K-joints.

Table 1. Geometric dimensions and dimensionless parameters of specimens.

Number	L	l	D	D_1	d	T	T_1	t	α	β	γ	τ	ζ
	mm	mm	mm	mm	mm	mm	mm	mm					
OC300-6-IC0-0-BR168-8-1	1800	485	300	-	168	6	-	8	12	0.56	25.00	1.33	-
OC300-6-IC0-0-BR168-8-2	1800	485	300	-	168	6	-	8	12	0.56	25.00	1.33	-
OC300-6-IC203-8-BR121-8	1800	485	300	203	121	6	8	8	12	0.40	25.00	1.33	0.715
OC300-10-IC203-8-BR102-14	1800	485	300	203	102	10	8	14	12	0.34	15.00	1.40	0.725
OC300-5-IC180-5-BR121-8	1800	485	300	180	121	5	5	8	12	0.40	30.00	1.60	0.621

Note: D is the diameter of the outer chord, T is the thickness of the outer chord, d is the diameter of the brace, t is the thickness of the brace, L is the axial length of the chord, and l is the axial length of the brace. D_1 and T_1 are the diameter and thickness of the inner chord, respectively, which are defined only for CFDST K-joints. β is the ratio of d to D, γ is the ratio of D to $2T$, τ is the ratio of t to T, and ζ is the hollow section ratio of the chord for CFDST K-joints.

The tensile test was carried out using the monotonic tensile machine of 100-kN-capacity at a room temperature of about 20 °C. Tensile coupons were cut from the chord and brace of the K-joints; detailed dimensions of tensile coupons designed according to ISO 6892-1 [25] are given in Figure 2 and Table 2, respectively. During the loading process, the deformation and applied load at the gauge length segment were measured using the extensometer and test machine, respectively. According to ISO 6892-1 [25] and the Huang [26], loading was controlled by the extensometer; the loading scheme is presented in Table 3. The strain rate was 0.000017 s^{-1} for the elastic stage, 0.00005 s^{-1} for the yield plateau stage, 0.0002 s^{-1} for the strain hardening stage, and 0.00033 s^{-1} for the necking stage. The measured engineering stress-strain curves are shown in Figure 3, and the mechanical properties of the tensile coupons are shown in Table 4. In the experiments, C50 concrete was utilized, with the mix proportions detailed in Table 5. To simulate the sealed environment post-concreting within the steel tube, concrete specimens were wrapped tightly with a plastic wrap after being cured with water for two days. Following a 28-day curing period in accordance with GB/T50081 [27], the cubic compressive strength of the self-compacting concrete was assessed using three 150 mm cubic specimens, yielding an average compressive strength of 72.1 MPa.

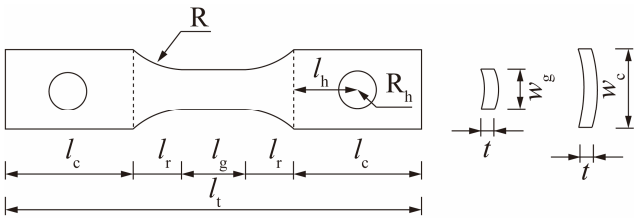

Figure 2. Dimensions of the tensile coupon specimens.

Table 2. Detailed dimensions of the tensile coupon specimens.

Member	Parameter	l_t/mm	l_r/mm	l_g/mm	l_c/mm	R/mm	t/mm	w_g/mm	w_c/mm	R_h/mm	l_h/mm	Number
Brace	168 × 8	214	15.0	64	60	15	8	10	35	6	30	2
	121 × 8	214	15.0	64	60	15	8	10	35	6	30	2
	102 × 14	213.6	14.8	64	60	15	14	6	30	6	30	2
	203 × 8	214	15.0	64	60	15	8	10	35	6	30	2
	180 × 5	214	15.0	64	60	15	5	16	45	6	30	2
Chord	300 × 5	214	15.0	64	60	15	5	16	45	6	30	2
	300 × 6	214	15.0	64	60	15	6	13	40	6	30	2
	300 × 10	213	14.5	64	60	15	10	8	30	6	30	2

Note: l_t is the total length of the tensile coupon specimens, l_r is the length of the transition arc segment, l_g is the gauge length of the specimen, l_c is the length of the clamping segment, R is the radius of transition arc, t is the thickness of the specimen, w_g is the width of the gauge segment, and w_c is the width of the clamping segment. R_h is the radius of the holes in the specimens, and l_h is the distance between the center of the hole and the end of the clamping segment.

Table 3. Strain rate of the tensile coupon test.

Stage	Strain Rate/s^{-1}
Elastic stage	0.000017
Yield plateau stage	0.00005
Strain hardening stage	0.0002
Necking stage	0.00033

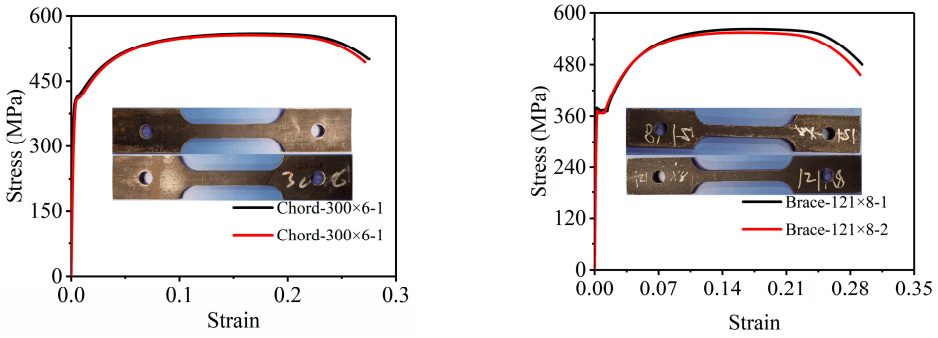

(**a**) Chord (**b**) Brace

Figure 3. Typical stress-strain curve of the materials for chord and brace.

Table 4. Mechanical properties of the tested Q355 steel.

Member	Specimen	Elastic Modulus/GPa	Yield Strength/MPa	Ultimate Strength/MPa
Chord	300 × 5-1	220.72	435.79	582.86
	300 × 5-2	223.37	435.71	571.33
	300 × 6-1	200.76	405.37	559.31
	300 × 6-2	197.37	394.75	556.34
	300 × 10-1	217.14	451.91	583.88
	300 × 10-2	213.15	449.59	586.35
Brace	121 × 8-1	215.64	371.00	563.29
	121 × 8-2	191.20	366.50	555.17
	203 × 8-1	199.53	427.83	591.27
	203 × 8-2	192.77	418.07	588.33
	102 × 14-1	230.66	347.06	546.45
	102 × 14-2	228.12	349.93	538.35
	180 × 5-1	231.44	361.26	576.74
	180 × 5-2	228.11	364.41	581.39
	168 × 8-1	226.83	389.49	553.76
	168 × 8-2	238.97	392.26	560.36

Table 5. Concrete mix ratio (kg/m^3).

Cement	Water	Fine Aggregate	Coarse Aggregate	Fly Ash	Water Reducer
392	145.6	681.5	1036.2	168	5.6

2.2. Test Setup

The schematic view and photo of the test setup to measure the SCF values of K-joints is shown in Figure 4. The chord of the K-joints was placed vertically, and both braces were hinged to supports. The actuator was fixed to the reaction steel frame and hinged to the end plate of the K-joints. The vertical load was applied at one end of the chord.

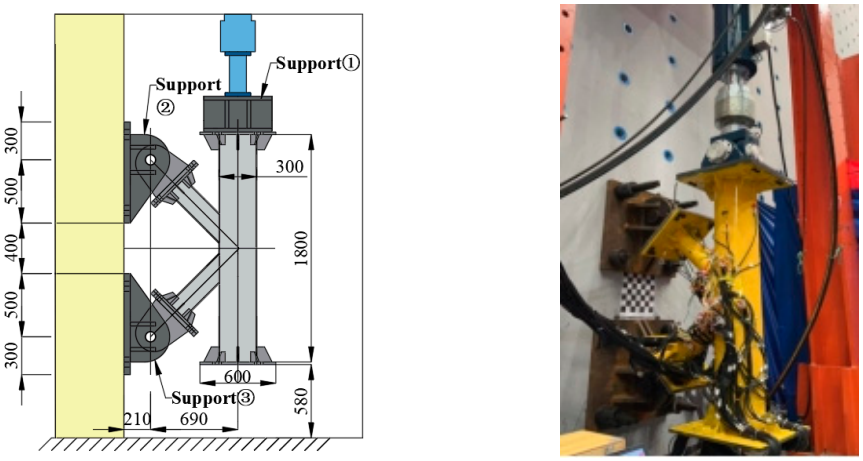

(**a**) Loading device (**b**) Specimen installation

Figure 4. Diagram of the test loading device and specimen installation.

In the test, the gradient strain gauge was used to measure the hot spot strain along the intersecting line near the welding toe. Each gradient strain gauge consisted of five biaxial strain gauges evenly distributed along the longitudinal direction, with a center spacing of 4 mm. The distance between the end of the gradient strain gauge and the end of the intersecting line was determined according to DNV [19], as shown in Figure 5. In addition, four uniaxial strain gauges were uniformly arranged at the position near the end of the tensile and compressive brace and the chord to measure the nominal strain of the chord and to calculate the actual load on applied specimens. According to CIDECT-8 [18], strain gauges of the brace were arranged along the axis of the brace, and strain gauges of the chord were arranged perpendicular to the weld seam. The overall arrangement of strain gauges and the angle of the measuring point Φ is shown in Figure 6.

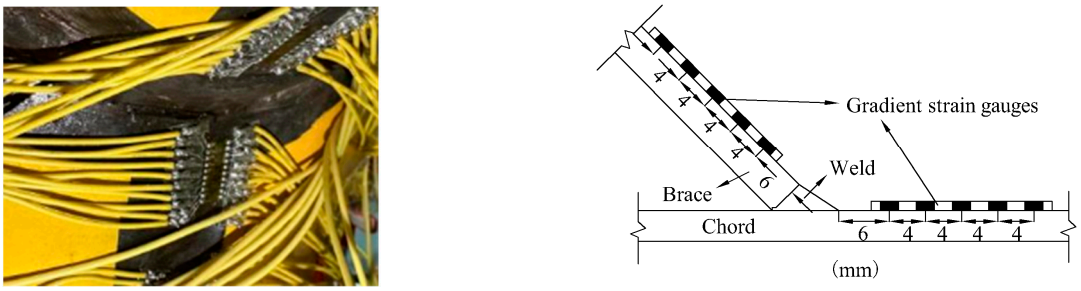

(**a**) Gradient strain gauge (**b**) Details of strain gauges adhesive

Figure 5. Layout of the gradient strain gauges.

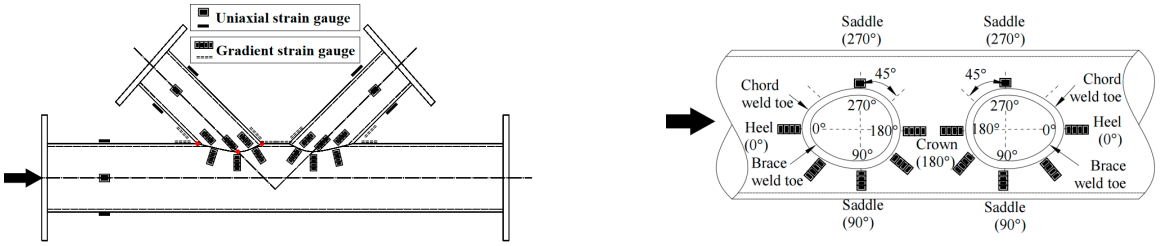

(**a**) The front view (**b**) The top view

Figure 6. Arrangement of strain gauges.

2.3. Measuring and Loading the System

Before the test, preloading was performed to ensure that the specimen was loaded within the linear elastic stage and to eliminate the influence of the installation gap. In the test, the load was applied in two stages, and displacement control was adopted with an actuator loading speed of 0.5 mm/min in the whole test. The test was stopped for 3 min when the specimens were loaded at 0.6 mm, 0.8 mm, and 1.0 mm, respectively, to obtained enough strain data in the stable loading period. Strains were continuously collected at a recording frequency of 20 Hz. The detailed loading scheme is shown in Figure 7.

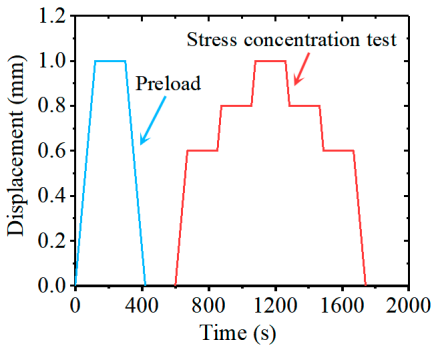

Figure 7. Loading scheme.

3. Test Results

3.1. General

To evaluate the influence of the inner concrete on the stress concentration of the K-joints, the hot spot stress of CHS and CFDST K-joints were compared based on the stress concentration factor (SCF). The SCF is defined as the ratio of hot spot stress to the corresponding nominal stress. For K-joints of the brace subjected to the axial load, the nominal stress can be obtained by the following Equation (2) [28]:

$$\sigma_{n,AX} = \frac{4F}{\left\{\pi\left[d^2 - (d-2t)^2\right]\right\}} \quad (2)$$

where $\sigma_{n,AX}$ is the nominal stress of the K-joint under axial force, F is the axial force, and d and t are the diameter and thickness of the brace, respectively.

Similarly, the strain concentration factor (SNCF) is defined as the ratio of hot spot strain to the corresponding nominal strain. A previous study recommended a relationship between SCF and SNCF for tubular joints, as shown in Equation (3) [29]. In the test, the parameter c can be determined by the ratio between the strain parallel to the weld and the strain perpendicular to the weld, as shown in Equation (4). The range of parameter c is usually between 1.1 and 1.2 [29]. In order to ensure the accuracy of the calculation and the correct evaluation of SCFs, the parameter c is taken as 1.2.

$$\mathrm{SCF} = c \cdot \mathrm{SNCF} \quad (3)$$

$$c = \frac{\left(1 + v\frac{\varepsilon_{//}}{\varepsilon_{\perp}}\right)}{(1 - v^2)} \quad (4)$$

where v is Poisson's ratio, and $\varepsilon_{//}$ and $\varepsilon_{\perp}$ are the strains parallel and perpendicular to the weld, respectively.

In the test, strain values at the mid-length of the brace and near the brace-chord intersection curves were obtained from arranged strain gauges, as shown in Figure 6. Thereafter, hot spot strains (ε_{hs}) were calculated by a linear extrapolation approach or quadratic extrapolation approach. These were converted to SCFs by the relationship between SCF and SNCF using Equation (3).

3.2. Extrapolation Method

In the test, the hot spot strain was obtained from the strain gauge reading, and was calculated by the linear or quadratic extrapolation approach. The quadratic extrapolation method can effectively process raw data, but the approach is sensitive to data errors. These errors might lead to the underestimation of SNCFs compared with the values obtained by the linear extrapolation approach [30]. Therefore, in this study, the linear extrapolation method was used to calculate SNCFs [23].

3.3. SCF Values

Both axial and bending stress on the chord are evitable during the test. Therefore, the total recorded hot spot stress ($\sigma_{hs,tot}$) consisted of the hot spot stress induced by the axial force and additional bending moment. The stress concentration factors of the CHS and CFDST K-joints were calculated using Equation (5), as shown in Table 6. The SCF distributions of both the brace and chord along the weld at the tensile side are shown in Figures 8 and 9, respectively.

$$SCF_{hs,tot} = SCF_{hs,ax} + SCF_{hs,ad} \quad (5)$$

Table 6. SCFs of CHS and CFDST K-joints.

Specimen No.		Tensile Side					Compressive Side				
		0°	**45°**	**90°**	**135°**	**180°**	**0°**	**45°**	**90°**	**135°**	**180°**
OC300−6−IC0−0−BR168−8−1	Chord	1.19	3.80	5.53	5.67	3.12	2.36	5.75	8.47	6.95	6.23
	Brace	0.46	0.97	2.13	2.30	1.72	0.34	2.02	2.47	1.87	1.80
OC300−6−IC0−0−BR168−8−2	Chord	1.23	4.12	6.16	5.73	3.08	2.39	4.80	9.00	8.08	5.82
	Brace	0.51	1.15	2.46	2.33	1.59	0.29	1.65	2.85	2.25	1.50
OC300−6−IC203−8−BR121−8	Chord	−1.16	−0.52	3.68	8.70	10.47	−2.26	−0.78	4.27	8.40	10.77
	Brace	0.32	0.47	0.63	0.94	3.26	0.58	1.81	2.26	2.09	3.54
OC300−10−IC203−8−BR102−14	Chord	−1.05	1.66	4.00	4.96	5.62	0.42	2.65	5.32	5.71	6.66
	Brace	0.45	0.59	0.69	1.75	2.80	0.33	1.26	1.66	2.41	2.65
OC300−5−IC180−5−BR121−8	Chord	0.82	1.76	5.33	13.39	10.70	2.33	4.48	13.53	14.10	13.71
	Brace	−0.05	0.49	0.93	1.58	4.30	−0.45	1.34	2.59	2.69	4.16

The maximum SCF values on the both tensile and compressive sides of OC300-6-IC0-0-BR168-8-1 were observed at 135° and 90° of the chord, respectively, as shown in Figure 8, while the position of the maximum SCF values of the chord at the tensile and compressive sides for the specimen OC300-6-IC0-0-BR168-8-2 altered to the 90° position, as shown in Figure 8. Furthermore, some discrepancy could be found for joints of the nominal same geometry, i.e., OC300-6-IC0-0-BR168-8-1 and OC300-6-IC0-0-BR168-8-2, as shown in Figure 8. This would be attributed to differences in these two joints from both the actual dimension and installation alignment.

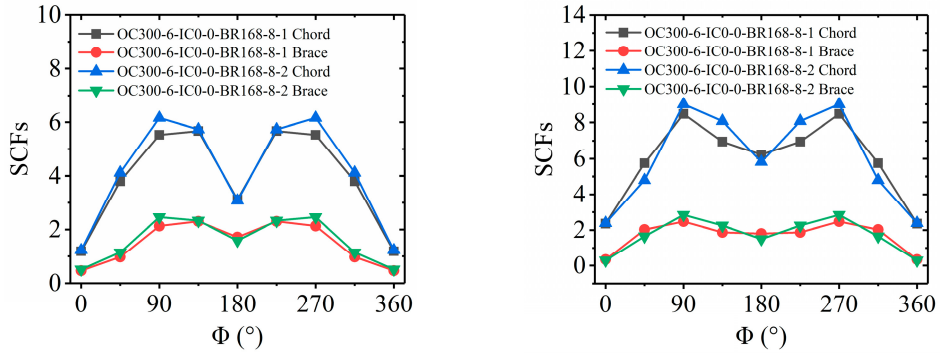

Figure 8. SCF distribution of the CHS joint.

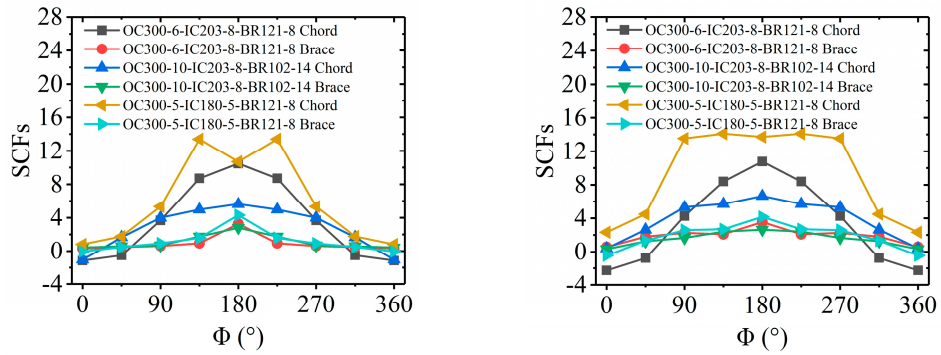

Figure 9. SCF distribution of the CFDST joint.

The distribution patterns of SCFs on the tensile and compressive sides of CFDST specimens OC300-6-IC203-8-BR121-8 and OC300-10-IC203-8-BR102-14 are fundamentally similar, with the peak SCF occurring at the 180° position along the chord, as shown in Figure 9. Although for specimen KC-3 both the maximum SCFs on the tension side and compression side are located at the 135°, there is a slight deviation in their distribution pattern. Notably, the SCF at the 90° position on the compression side is significantly greater than that on the tension side. This variation may be attributed to minor differences in the weld geometry between the tension and compression sides, resulting from manufacturing tolerances.

Furthermore, upon comparing SCF distributions in CFDST joints versus those in CHS joints, it becomes evident that the adoption of CFDST has altered SCF distribution characteristics. In the case of OC300-6-IC203-8-BR121-8 and OC300-10-IC203-8-BR102-14, the highest SCFs in both the chord and brace are consistently found at the 180°. By contrast, for the CHS joints, these maxima occur at different locations.

In summary, while there is consistency in the overall SCF distribution pattern among certain CFDST specimens, deviations have been observed in OC300-5-IC180-5-BR121-8, potentially due to fabrication inconsistencies, and a clear distinction in SCF behavior is seen when contrasting CFDST nodes with conventional CHS ones, highlighting the influence of CFDST geometry on stress concentration phenomena.

4. Numerical Modelling of CFDST K-Joints

4.1. General

For welded tubular joints, the weld makes the geometric shape transition more smoothly at the intersection line, leading to a reduced stress concentration near the intersecting line. The brace-to-chord intersecting line is an intricate spatial curve, which would cause meticulous simulation of the weld joint for an accurate finite element analysis. As

shown in Figure 10, the weld of the tubular K-joint adheres to the AWS code [31], specifying distinct weld sections at various positions between the brace and chord. The weld section can be comprehensively characterized by calculating weld size T_2 at the weld root and weld size T_3 at the weld toe. Additionally, A_0 and A_i denote the exterior and interior intersection points, respectively, of the intersection section between the brace and chord. Furthermore, W_0 and W_i represent the intersection points of the weld toe and the weld root on this particular section, respectively. Meanwhile, the configuration of the weld section varies depending on its location and is intimately linked to the angle ω formed between the tube walls of the brace and chord at that particular cross-section. Figure 10a,b presents the cross-section of the welds under two scenarios, with ω exhibiting non-obtuse and obtuse characteristics, respectively, for varying angles θ between the brace and chord. At the angle θ of 45°, ω is equal to 135° and 45° at the heel and crown point, respectively. Conversely, at the saddle points on both sides, ω remains steady at 90°, displaying a consistent geometric feature.

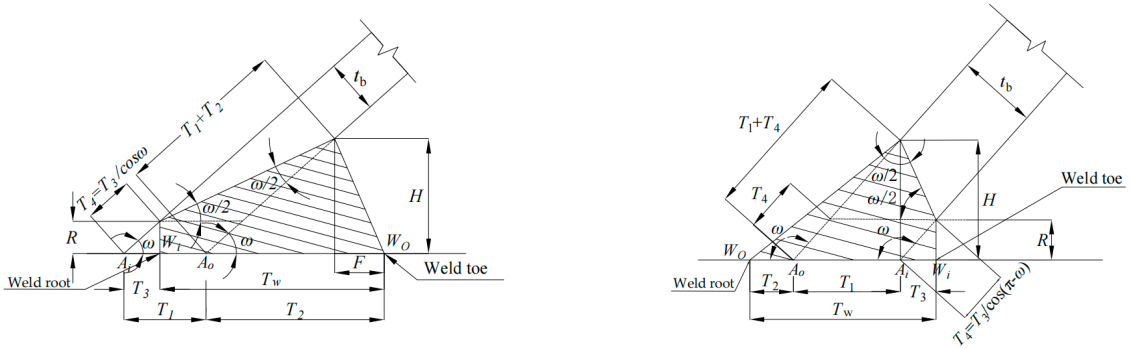

(**a**) $0° < \omega \leq 90°$ (**b**) $90° < \omega < 180°$

Figure 10. Weld simulation.

As recommended by the AWS code [31], weld size T_2 at the weld root and T_3 at the weld toe can be accurately derived through meticulous geometric relationships. The comprehensive derivation process leads to the following conclusive results:

$$T_3 = R\cot\omega \tag{6}$$

$$T_2 = (T_1 + T_4)\cos\omega + F = (t_b + R)\cot\omega + F \tag{7}$$

where AWS code suggests R ranges from 2 to 6 mm, and F takes $t_b/2$.

Considering geometric dimensions of welded joints, a sophisticated finite element model of the CHS and CFDST K-joints was constructed utilizing the SOLID element (C3D8I) within the finite element software ABAQUS 6.14-4. This element type exhibits a high degree of accuracy in stress computations and is suitable for analyzing stress concentration issues. The tubular joint model adopts an integral modeling approach, where nodes are shared among various components, aligning with the actual welding process. The sandwich concrete and inner tube are modeled separately and then assembled with the hollow section tubular joint. The relevant parameters of the tubular joint are defined, as shown in Figure 1, while the finite element model of the tubular joint is presented in Figure 11. The cross-section of the weld is presented in Figure 12.

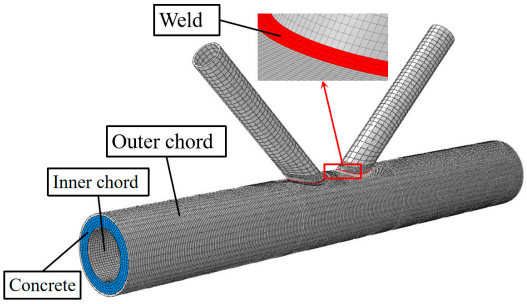

Figure 11. The finite element model.

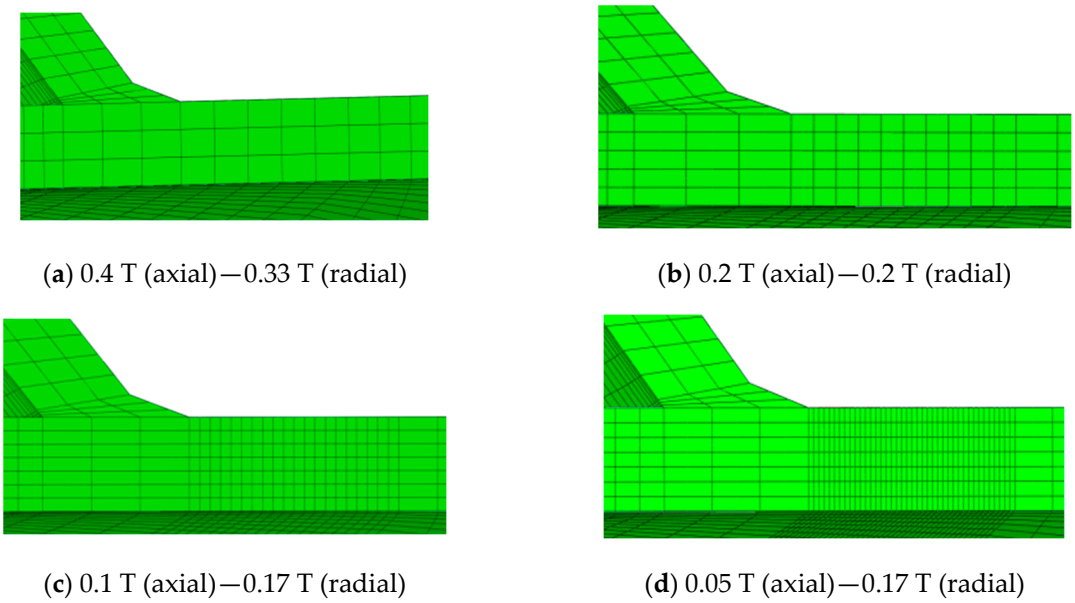

(**a**) 0.4 T (axial)—0.33 T (radial)

(**b**) 0.2 T (axial)—0.2 T (radial)

(**c**) 0.1 T (axial)—0.17 T (radial)

(**d**) 0.05 T (axial)—0.17 T (radial)

Figure 12. Different mesh density near weld toe.

In this present study, the contact interface between the steel tube and the sandwiched concrete in the grouted welded joint specimens is modeled under the following assumptions: a hard contact in the normal direction, precluding any penetration but excluding normal bond stress; and a frictional contact in the tangential direction, with a friction coefficient ranging between 0.2 and 0.6. In this study, 0.6 for the friction coefficient was adopted [32]. Notably, the tangential friction stress is not only determined by the product of the friction coefficient and normal stress, but is also constrained by a minimum threshold, which corresponds to the tangential bond stress calculated using Equation (8):

$$\tau_{\text{bond}} = 2.314 - 0.0195(D/T) \tag{8}$$

The boundary constraints and loading conditions of the model are meticulously designed in accordance with the experimental configuration. In the finite element analysis of the stress field proximate to welded tubular joints, the mesh generation process was carefully tailored to optimize the trade-off between computational precision and efficiency. Specifically, a zonal meshing strategy was implemented, with dense meshing in regions exhibiting pronounced stress concentration, particularly at and adjacent to weld seams and sparse meshing in areas with more gradual stress gradients.

A mesh sensitivity analysis was conducted in the vicinity of the weld seam to assess the impact of mesh refinement on the computation of hot spot stress. As depicted in Figures 12 and 13, stress concentration factors were computed for various mesh sizes, specifically 0.4 T (axial)—0.33 T (radial), 0.2 T (axial)—0.2 T (radial), 0.1 T (axial)—0.17 T (radial) and 0.05 T (axial)—0.17 T (radial). The results revealed that larger mesh sizes led to

greater sensitivity in computed outcomes. However, as the mesh size decreased below 0.2 t, the influence on computational results became increasingly negligible. To strike a balance between computational accuracy and efficiency, a mesh size of 0.1 T (axial)—0.17 T (radial) was chosen for subsequent numerical simulations. The mesh in the non-interpolated area proximate to the weld seam measured approximately 0.5 T. Areas distant from the weld seam, characterized by minimal stress levels, were designated as sparsely meshed regions, with their impact on the overall computational results deemed insignificant.

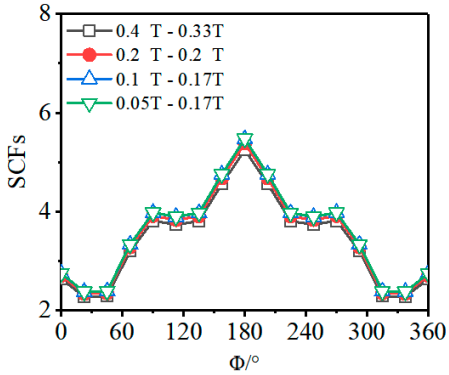

Figure 13. Grid sensitivity analysis.

4.2. Material Properties

Within the ABAQUS computational environment, the accuracy of the numerical analysis results hinges on the precise definition of input stress-strain data. For steel, a plasticity model was employed to depict its behavior, with an elastic modulus of 210 GPa and a Poisson's ratio of 0.3. For concrete, given its complex fracture modes that can lead to brittle failure at low stress levels, a plastic-damage model was selected to simulate its non-linear behavior. The elastic modulus and Poisson's ratio for concrete were taken as 34.5 GPa and 0.2, respectively. The material properties of concrete were defined by integrating experimental data with the constitutive model proposed by Han [33]; detailed parameters are shown in reference [34]. This approach ensures a comprehensive representation of concrete's behavior in the ABAQUS model.

$$y = \begin{cases} 2x - x^2 & (x \le 1) \\ \frac{x}{\beta_0 (x-1)^{\varphi} + x} & (x \ge 1) \end{cases} \tag{9}$$

$$x = \frac{\varepsilon}{\varepsilon_0}, y = \frac{\sigma}{\sigma_0} \tag{10}$$

$$\sigma_0 = f_c' \tag{11}$$

$$\varepsilon_0 = \varepsilon_c + 800 \cdot \mu^{0.2} \cdot 10^{-6} \tag{12}$$

$$\varepsilon_c = \left(1300 + 12.5 f_c'\right) \cdot 10^{-6} \tag{13}$$

$$\beta_0 = 0.0000236^{[0.25+(\mu-0.5)^{0.7}]} \cdot \left(f_c'\right)^{0.5} \cdot 0.5 \ge 0.12 \tag{14}$$

where f_c' is the compressive strength of cylindrical concrete specimens, $\varphi = 2$ and μ is the coefficient pertaining to confinement effects:

$$\mu = \frac{A_s f_y}{A_c f_{ck}} \tag{15}$$

where A_s represents the cross-sectional area of the external steel tube, whereas f_y signifies its yield strength. A_c is the cross-sectional area of the hollow portion within the confines of the external steel tube, and f_{ck} corresponds to the characteristic axial compressive strength of the concrete.

4.3. Validations

Validations of the findings were conducted utilizing experimental data derived from the current research endeavor. Presented in Table 7 are geometric parameters associated with tubular joint configurations, and corresponding computational results. Notably, SCF_{FE} signifies the outcomes obtained through the FE analysis, while SCF_{Test} represents the experimentally derived data.

Table 7. Comparison of results between SCF_{FE} and SCF_{Test}.

No.		SCF_{FE}					SCF_{Test}				
Tensile Side		**0°**	**45°**	**90°**	**135°**	**180°**	**0°**	**45°**	**90°**	**135°**	**180°**
OC300−6−IC0−0−BR168−8−1	Chord	1.13	2.86	7.16	5.09	3.89	1.19	3.80	5.53	5.67	3.12
	Brace	0.09	1.01	2.44	2.14	1.19	0.46	0.97	2.13	2.30	1.72
OC300−6−IC0−0−BR168−8−2	Chord	1.13	2.86	7.16	5.09	3.89	1.23	4.12	6.16	5.73	3.08
	Brace	0.09	1.01	2.44	2.14	1.19	0.51	1.15	2.46	2.33	1.59
OC300−6−IC203−8−BR121−8	Chord	−1.95	−0.83	5.22	7.35	11.38	−1.16	−0.52	3.68	8.70	10.47
	Brace	0.19	0.42	0.52	1.17	3.40	0.32	0.47	0.63	0.94	3.26
OC300−10−IC203−8−BR102−14	Chord	−0.15	1.02	3.63	3.86	5.24	−1.05	1.66	4.00	4.96	5.62
	Brace	0.55	0.71	0.84	1.68	2.95	0.45	0.59	0.69	1.75	2.80
OC300−5−IC180−5−BR121−8	Chord	0.64	2.20	6.62	15.89	10.47	0.82	1.76	5.33	13.39	10.70
	Brace	−0.06	0.50	0.81	1.44	3.82	−0.05	0.49	0.93	1.58	4.30
Compressive side		0°	45°	90°	135°	180°	0°	45°	90°	135°	180°
OC300−6−IC0−0−BR168−8−1	Chord	2.50	3.58	7.69	6.51	5.79	2.36	5.75	8.47	6.95	6.23
	Brace	0.15	1.47	2.79	2.39	1.13	0.34	2.02	2.47	1.87	1.80
OC300−6−IC0−0−BR168−8−2	Chord	2.50	3.58	7.69	6.51	5.79	2.39	4.80	9.00	8.08	5.82
	Brace	0.15	1.47	2.79	2.39	1.13	0.29	1.65	2.85	2.25	1.50
OC300−6−IC203−8−BR121−8	Chord	−1.32	−1.00	4.86	7.10	11.37	−2.26	−0.78	4.27	8.40	10.77
	Brace	0.21	1.31	1.82	2.12	3.47	0.58	1.81	2.26	2.09	3.54
OC300−10−IC203−8−BR102−14	Chord	1.44	2.55	5.11	5.71	6.85	0.42	2.65	5.32	5.71	6.66
	Brace	0.37	1.47	1.64	2.24	3.14	0.33	1.26	1.66	2.41	2.65
OC300−5−IC180−5−BR121−8	Chord	1.82	5.21	9.44	14.35	13.64	2.33	4.48	13.53	14.10	13.71
	Brace	−0.35	1.36	2.06	2.13	3.29	−0.45	1.34	2.59	2.69	4.16

As shown in Figure 14, a comparative analysis was conducted juxtaposing the experimental results against the FE outcomes. It is evident that the FE computations exhibit substantial concurrence with the experimental data. To enhance the precision of the comparison and to assess the validity of stress concentration factors derived from the hot spot stress approach, Table 8 provides the ratios of FE results to experimental outcomes (SCF_{FE}/SCF_{Test}). Furthermore, this table incorporates the mean and coefficient of variation (CV) of the stress concentration factor ratios calculated using the hot spot stress approach. The mean SCF_{FE}/SCF_{Test} ratio for CHS joints ranges from 0.85 to 1.05, while for CFDST joints, it spans from 0.81 to 1.24. Collectively, the reported mean values fall within an acceptable parameter range. Moreover, given the notably small SCFs values observed at the 0° position, these data points were not taken into account during the computation of the statistical mean and CV.

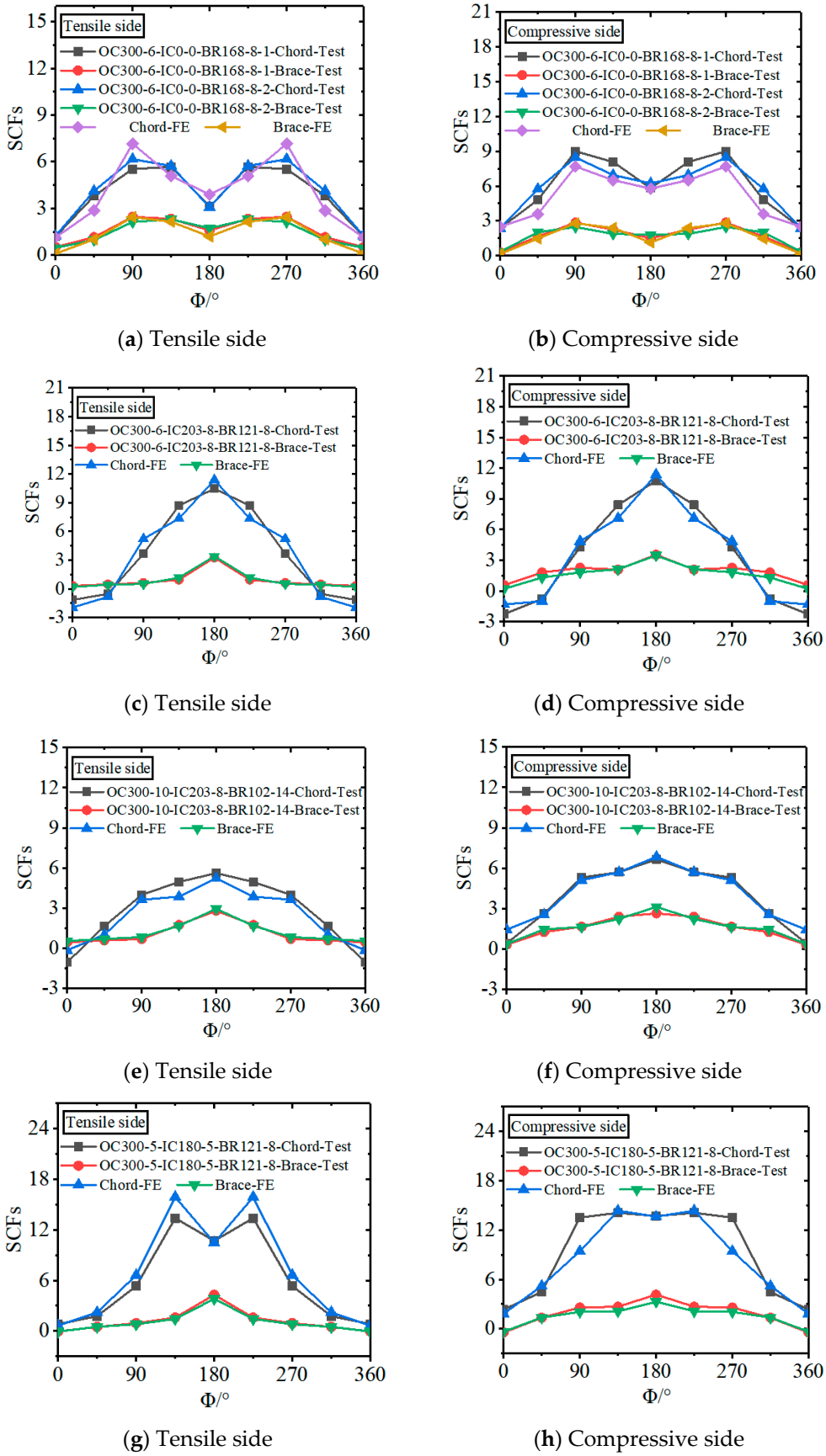

Figure 14. Comparison of results between SCF_{FE} and SCF_{Test}.

Table 8. Comparison of errors between SCF_{FE} and SCF_{Test} results.

No.		SCF_{FE}/SCF_{Test}					Average	CV
Tensile Side		**0°**	**45°**	**90°**	**135°**	**180°**		
OC300-6-IC0-0-BR168-8-1	Chord	0.95	0.75	1.29	0.90	1.25	1.05	0.22
	Brace	0.20	1.04	1.15	0.93	0.69	0.95	0.14
OC300-6-IC0-0-BR168-8-2	Chord	0.92	0.69	1.16	0.89	1.26	1.00	0.21
	Brace	0.18	0.88	0.99	0.92	0.75	0.88	0.07
OC300-6-IC203-8-BR121-8	Chord	1.68	1.60	1.42	0.84	1.09	1.24	0.27
	Brace	0.59	0.89	0.83	1.24	1.04	1.00	0.14
OC300-10-IC203-8-BR102-14	Chord	0.14	0.61	0.91	0.78	0.93	0.81	0.11
	Brace	1.22	1.20	1.22	0.96	1.05	1.11	0.10
OC300-5-IC180-5-BR121-8	Chord	0.78	1.25	1.24	1.19	0.98	1.16	0.09
	Brace	1.20	1.02	0.87	0.91	0.89	0.92	0.05
Compressive side		0°	45°	90°	135°	180°		
OC300-6-IC0-0-BR168-8-1	Chord	1.06	0.62	0.91	0.94	0.93	0.85	0.11
	Brace	0.44	0.73	1.13	1.28	0.63	0.94	0.26
OC300-6-IC0-0-BR168-8-2	Chord	1.05	0.75	0.85	0.81	0.99	0.85	0.07
	Brace	0.52	0.89	0.98	1.06	0.75	0.92	0.10
OC300-6-IC203-8-BR121-8	Chord	0.58	1.28	1.14	0.85	1.06	1.08	0.13
	Brace	0.36	0.72	0.81	1.01	0.98	0.88	0.12
OC300-10-IC203-8-BR102-14	Chord	3.43	0.96	0.96	1.00	1.03	0.99	0.03
	Brace	1.12	1.17	0.99	0.93	1.18	1.07	0.11
OC300-5-IC180-5-BR121-8	Chord	0.78	1.16	0.70	1.02	0.99	0.97	0.14
	Brace	0.78	1.01	0.80	0.79	0.79	0.85	0.08

5. Parametric Study

5.1. General

The diameter ratio of brace-to-chord β, the chord radius-to-thickness ratio γ, the thickness ratio of brace-to-chord τ, and the brace-to-chord angle θ have significant effects on the hot spot SCF of CHS K-joints, according to previous research [20,35].

Moreover, when the brace is subjected to tension or compression, the section of the chord of CHS K-joints may appear to have local outward deformation, as shown in Figure 15. For the CFDST-K joint, the inner filled concrete would increase the radius stiffness of the chord, thereby reducing the overall deformation of the CFDST K-joints and improving the stress concentration in the joint core area, as shown in Figure 15. Therefore, the influence of geometrical parameters, i.e., the diameter ratio of brace-to-chord β, the chord radius-to-thickness ratio γ, the thickness ratio of brace-to-chord τ, the brace-to-chord angle θ, and the hollow section ratio ζ of the CFDST K-joints, on the value and distribution of the SCF for K-joints was assessed. It should be noted that fatigue failure would be generally caused by tensile stress [36–38], and therefore, this study only focused on SCFs on the tensile side of K-joints.

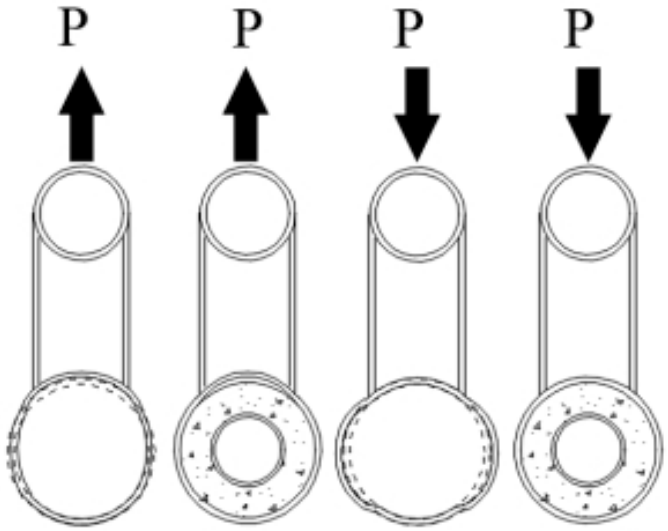

Figure 15. Diagram of chord section deformation of CHS and CFDST K-joints.

The angle values along the circle of the intersecting line are defined in Figure 16. It could be identified that the positions of 0°, 90°, and 180°are the crown heel, saddle, and crown toe of the intersecting line. In this study the change in the hollow section ratio was achieved by changing the thickness of the concrete and the diameter of the inner steel tube, and the K-joint with the hollow section ratio of 0.915 is determined as the benchmarked joint to assess the influence of the ratios of β, γ, τ, θ, and ζ on the hot spot SCF of K-joints. Furthermore, the degradation ratio η was defined as the ratio of the maximum hot spot SCF of the CFDST K-joint to that of the CHS K-joint, which can be calculated using Equation (16). Detailed geometric dimensions of the studied K-joints are shown in Figure 17 and are listed in Table 9. The total of the numerical models was 51 groups, including 22 groups of the CHS K-joints and 29 groups of CFDST K-joints. The tested material properties of Q355 steel and C50 self-compacting mortar concrete were used in this study.

$$\eta = SCF_{\mathrm{CFDST,max}} / SCF_{\mathrm{CHS,max}} \tag{16}$$

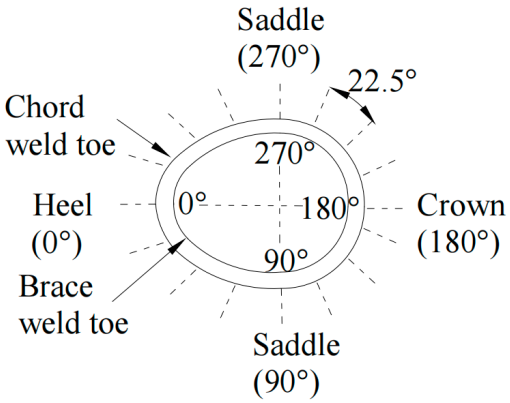

Figure 16. Angle distribution along the circle of the intersecting line.

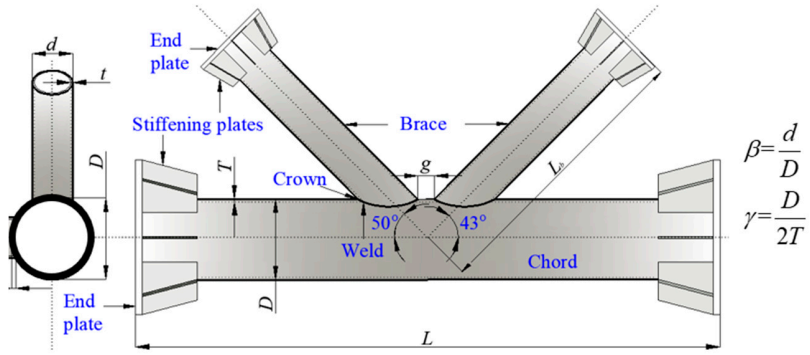

(**a**) CHS K-joints

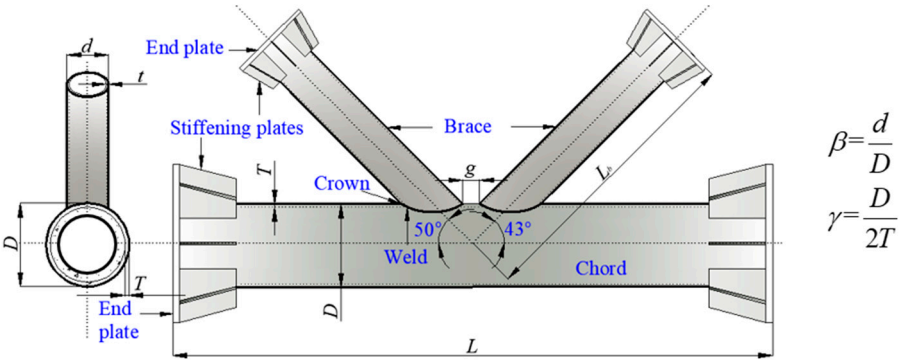

(**b**) CFDST K-joints

Figure 17. Diagram of a CHS K-joint and a CFDST K-joint.

Table 9. Detailed dimensions of studied K-joints.

Joint	Number	Variable	D	D_1	d	T	T_1	t	d/D	D/2T	t/T	θ	ζ
CHS K-joints	K-FE-1	β = d/D	300	-	60	8	-	8	0.2	18.75	1	45	-
	K-FE-2		300	-	90	8	-	8	0.3	18.75	1	45	-
	K-FE-3		300	-	120	8	-	8	0.4	18.75	1	45	-
	K-FE-4		300	-	150	8	-	8	0.5	18.75	1	45	-
	K-FE-5		300	-	180	8	-	8	0.6	18.75	1	45	-
	K-FE-6		300	-	210	8	-	8	0.7	18.75	1	45	-
	K-FE-7		300	-	240	8	-	8	0.8	18.75	1	45	-
	K-FE-8	γ = D/2T	300	-	120	4	-	4	0.4	37.5	1	45	-
	K-FE-9		300	-	120	5	-	5	0.4	30	1	45	-
	K-FE-10		300	-	120	6	-	6	0.4	25	1	45	-
	K-FE-11		300	-	120	10	-	10	0.4	15	1	45	-
	K-FE-12		300	-	120	12	-	12	0.4	12.5	1	45	-
	K-FE-13		300	-	120	14	-	14	0.4	10.71	1	45	-
	K-FE-14		300	-	120	16	-	16	0.4	9.38	1	45	-
	K-FE-15	τ = t/T	300	-	120	8	-	4	0.4	18.75	0.5	45	-
	K-FE-16		300	-	120	8	-	6	0.4	18.75	0.75	45	-
	K-FE-17		300	-	120	8	-	10	0.4	18.75	1.25	45	-
	K-FE-18		300	-	120	8	-	12	0.4	18.75	1.5	45	-
	K-FE-19	θ	300	-	120	8	-	8	0.4	18.75	1	30	-
	K-FE-20		300	-	120	8	-	8	0.4	18.75	1	40	-
	K-FE-21		300	-	120	8	-	8	0.4	18.75	1	50	-
	K-FE-22		300	-	120	8	-	8	0.4	18.75	1	60	-

Table 9. *Cont.*

Joint	Number	Variable	D	D_1	d	T	T_1	t	d/D	D/2T	t/T	θ	ζ
CFDST K-joints	K-FE-23	β = d/D	300	260	60	8	4	8	0.2	18.75	1	45	0.915
	K-FE-24		300	260	90	8	4	8	0.3	18.75	1	45	0.915
	K-FE-25		300	260	120	8	4	8	0.4	18.75	1	45	0.915
	K-FE-26		300	260	150	8	4	8	0.5	18.75	1	45	0.915
	K-FE-27		300	260	180	8	4	8	0.6	18.75	1	45	0.915
	K-FE-28		300	260	210	8	4	8	0.7	18.75	1	45	0.915
	K-FE-29		300	260	240	8	4	8	0.8	18.75	1	45	0.915
	K-FE-30	γ = D/2T	300	267.32	120	4	4	4	0.4	37.5	1	45	0.915
	K-FE-31		300	265.49	120	5	4	5	0.4	30	1	45	0.915
	K-FE-32		300	263.66	120	6	4	6	0.4	25	1	45	0.915
	K-FE-33		300	256.34	120	10	4	10	0.4	15	1	45	0.915
	K-FE-34		300	252.68	120	12	4	12	0.4	12.5	1	45	0.915
	K-FE-35		300	249.01	120	14	4	14	0.4	10.71	1	45	0.915
	K-FE-36		300	245.35	120	16	4	16	0.4	9.38	1	45	0.915
	K-FE-37	τ = t/T	300	260	120	8	4	4	0.4	18.75	0.5	45	0.915
	K-FE-38		300	260	120	8	4	6	0.4	18.75	0.75	45	0.915
	K-FE-39		300	260	120	8	4	10	0.4	18.75	1.25	45	0.915
	K-FE-40		300	260	120	8	4	12	0.4	18.75	1.5	45	0.915
	K-FE-41	θ	300	260	120	8	4	8	0.4	18.75	1	30	0.915
	K-FE-42		300	260	120	8	4	8	0.4	18.75	1	40	0.915
	K-FE-43		300	260	120	8	4	8	0.4	18.75	1	50	0.915
	K-FE-44		300	260	120	8	4	8	0.4	18.75	1	60	0.915
	K-FE-45	ζ	300	260	120	8	4	8	0.4	18.75	1	45	0.915
	K-FE-46		300	230	120	8	4	8	0.4	18.75	1	45	0.81
	K-FE-47		300	200	120	8	4	8	0.4	18.75	1	45	0.704
	K-FE-48		300	170	120	8	4	8	0.4	18.75	1	45	0.599
	K-FE-49		300	140	120	8	4	8	0.4	18.75	1	45	0.493
	K-FE-50		300	120	120	8	4	8	0.4	18.75	1	45	0.423
	K-FE-51		300	90	120	8	4	8	0.4	18.75	1	45	0.317

5.2. Effect of Hollow Section Ratio ζ

The distribution of the hot spot SCF along the circle of the intersecting line of the brace and chord, and the magnitude of the hot spot SCF of the crown heel, saddle, and crown toe of the intersecting line are shown in Figure 18a,b, respectively. The range of the hollow section ratio ζ was 0.317 to 0.915, and the rest of the variables β, γ, τ, and θ remained constant, as shown in models K-FE-45 to K-FE-45 in Table 9. It can be found that the hollow section ratio has little influence on the distribution of the hot spot SCF. With the decrease in hollow section ratio, the decreasing trend of hot spot SCFs at positions of crown heel, saddle, and crown toe gradually becomes stable. This may be due to the improved ability of the inner concrete and steel tube to resist deformation as the hollow section ratio decreases. When the hollow section ratio is gradually reduced, the inner concrete and steel tube can significantly increase the stiffness of the chord, thereby reducing the section deformation of the chord and the hot spot SCF in the CFDST K-joint core area. It should be noted that when the hollow section ratio is reduced to less than 0.7, the distribution and magnitude of the hot spot SCF of the CFDST K-joint may be close to that of the fully filled concrete K-joints.

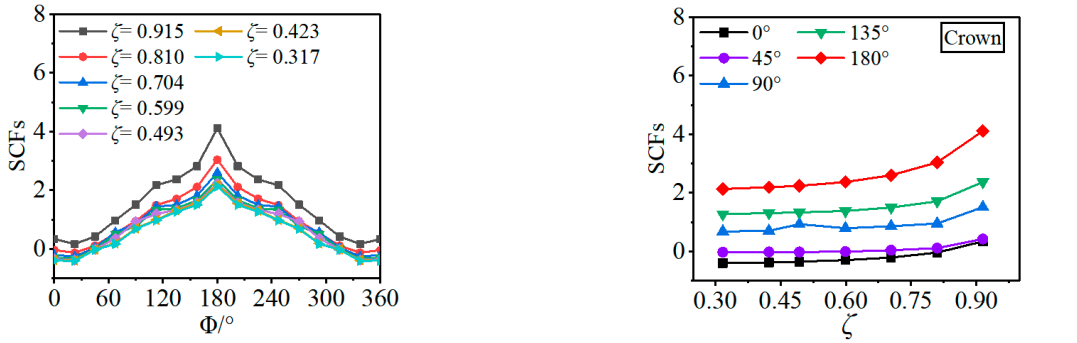

(**a**) The distribution of the hot spot SCF (**b**) The magnitude of the hot spot SCF

Figure 18. Effect of ζ on hot spot SCFs.

The degradation ratio η of the hot spot SCF with different hollow section ratios is shown in Figure 19, where a hollow section ratio of 1.0 means the CHS K-joints, and a hollow section ratio of less than 1.0 means the CFDST K-joint. It can be seen that when the hollow section ratio is less than 0.915, the degradation ratio is about 0.45. The hot spot SCF can be significantly decreased by the CFDST K-joint compared to that of the CHS K-joints.

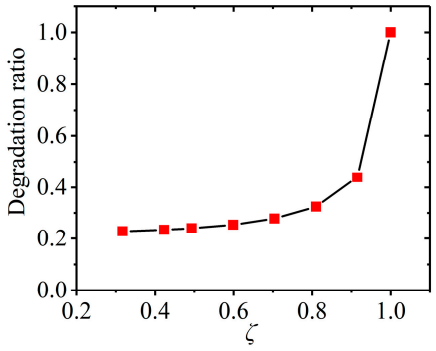

Figure 19. Degradation ratio of the hot spot SCF at different ratios ζ.

5.3. Effect of the Ratio of Diameter of the Brace to That of Chord β

Figure 20 shows the relationship between the diameter ratio of brace-to-chord β and the hot spot SCF at the intersecting line weld of CHS and CFDST K-joints. The range of the hollow section ratio β was 0.2 to 0.8, and the rest of the variables γ, τ, θ, and ζ remained constant, as shown in models K-FE-1 to K-FE-7 for CHS K-joints and K-FE-23 to K-FE-29 for CFDST K-joints in Table 9. The distribution trend of hot spot SCFs of CHS and CFDST K-joints is identical. The hot spot SCFs increase with the angle of the intersecting line with the range of 0 to 180°. Figure 21 reports the magnitude of the hot spot SCF at the positions of crown heel, saddle, and crown toe of the intersecting line. For CHS k-joints, when ratio β is greater than 0.3, hot spot SCFs basically keep stable. However, for CFDST K-joints, when ratio β is greater than 0.7, hot spot SCFs significantly decrease with ratio β increasing, indicating that the effects of ratio β on hot spot SCFs of CFDST K-joints is greater than those of CHS k-joints. Moreover, the magnitude of the hot spot SCF of CFDST K-joints is significantly less than that of CHS K-joints.

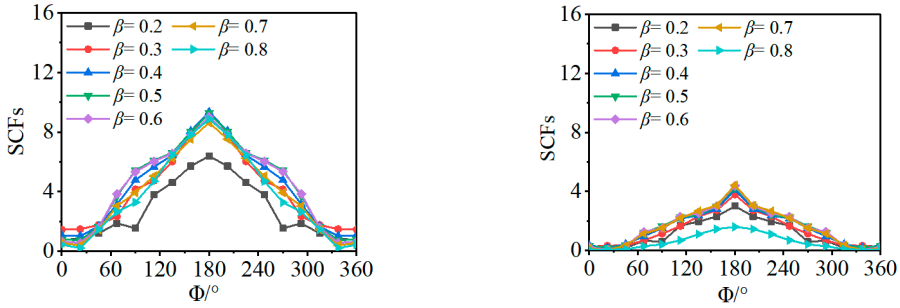

(**a**) CHS K-joint (**b**) CFDST K-joint

Figure 20. Distribution of the hot spot SCF of K-joints.

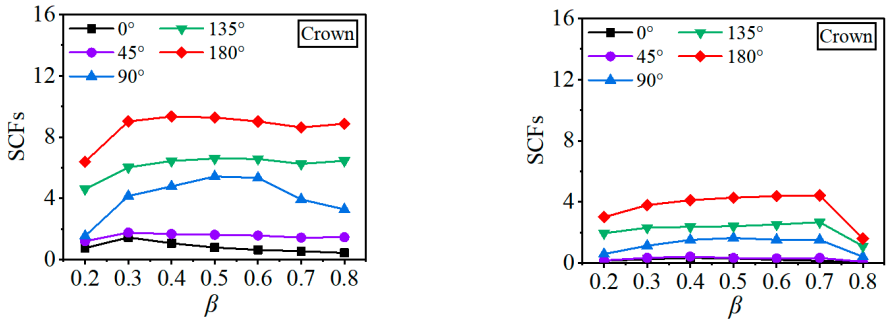

(**a**) CHS K-joint (**b**) CFDST K-joint

Figure 21. Magnitude of the hot spot SCF of K-joints.

The degradation ratio η of the hot spot SCF with a different ratio β is shown in Figure 22. When ratio β is less than 0.7, the degradation remains stable at 0.4-0.5. With the ratio β increase to 0.8, the degradation ratio decreases to about 0.2. That is, CFDST K-joints with a large ratio β can clearly decrease the hot spot SCF.

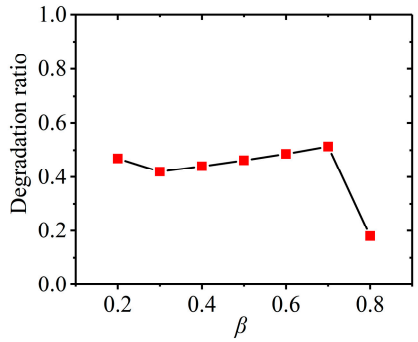

Figure 22. Degradation ratio of the hot spot SCF at a different ratio β.

5.4. Effect of the Ratio of Radius to Thickness of Chord γ

Figure 23 shows the relationship between the chord radius-to-thickness ratio γ and the hot spot SCF at the intersecting line weld of CHS and CFDST K-joints. The range of the hollow section ratio γ was 9.38 to 37.5, and the rest of the variables β, τ, θ, and ζ remained constant, as shown in models K-FE-8 to K-FE-14 and K-FE-30 for CHS K-joints to K-FE-36 for CFDST K-joints in Table 9. The distribution trend of the hot spot SCFs of CHS and CFDST K-joints is the same. Figure 24 illustrates the magnitude of the hot spot SCF at the positions of the crown heel, saddle, and crown toe of the intersecting line. The hot spot SCF at the position of the crown toe (180°) is the maximum, but that at the position of the crown heel (0°) is the minimum. For the CHS k-joint, the hot spot SCF at the position of the crown toe increases, with ratio γ increasing. However, when the ratio γ is greater than 25,

the hot spot SCF at the position of the crown toe of CFDST K-joints significantly decreases, with ratio γ increasing. That is, the increase in the hot spot SCF caused by reducing the wall thickness or increasing the diameter of the chord can be weakened by grouting the CFDST K-joints.

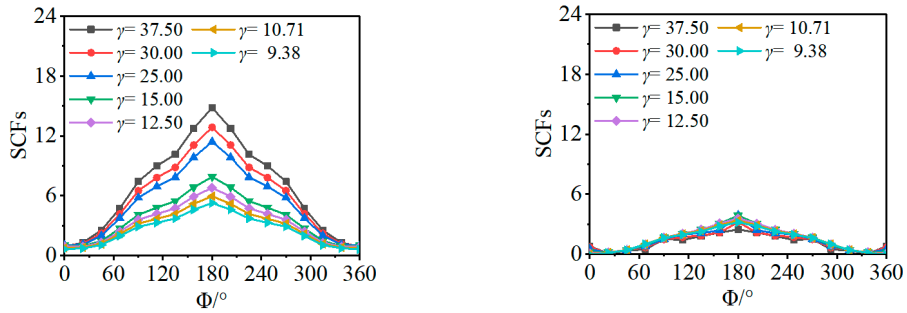

Figure 23. Distribution of the hot spot SCF of K-joints.

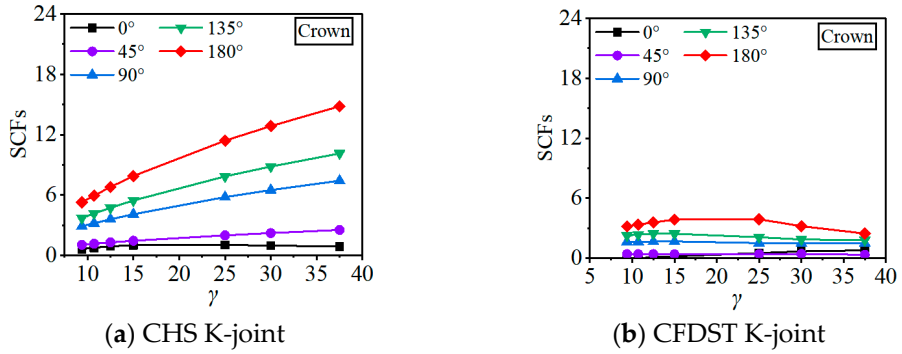

Figure 24. Magnitude of the hot spot SCF of K-joints.

Figure 25 shows the degradation ratio η of the hot spot SCF at different ratios γ. It was found that the degradation ratio η decreased linearly with an increase in ratio γ. When ratio γ is 37.50, the degradation ratio η is 0.2. That means the maximum hot spot SCF of the CFDST K-joints decreases by up to 80% compared to that of the CHS K-joints. Therefore, CFDST K-joints with a large ratio γ can significantly decrease the maximum hot spot SCF.

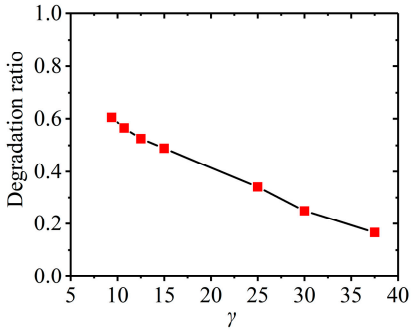

Figure 25. Degradation ratio of the hot spot SCF at different ratios γ.

5.5. Effect of the Ratio of Thickness of the Brace to That of Chord τ

The relationship between the thickness ratio of brace-to-chord τ and the hot spot SCF at the intersecting line weld of CHS and CFDST K-joints is shown in Figure 26. The range of the hollow section ratio τ was 0.5 to 1.5, and the rest of the variables β, γ, θ, and ζ remained constant, as shown in models K-FE-15 to K-FE-18 for CHS K-joints and K-FE-37 to K-FE-40 for CFDST K-joints in Table 9. The distribution trend of the hot spot SCFs of CHS and

CFDST K-joints is similar. The magnitude of the hot spot SCF at the positions of the crown heel, saddle, and crown toe of the intersecting line is illustrated in Figure 27. With ratio τ increasing, the hot spot SCF of CHS and CFDST K-joints increases linearly. However, the increasing rate of the hot spot SCF of CFDST K-joints is less than that of CHS K-joints. Figure 28 shows the degradation ratio η of the maximum hot spot SCF of CFDST K-joints compared to CHS K-joints. Ratio η basically remains stable with a value of 0.45, with ratio τ increasing. The influence of ratio τ on the maximum hot spot SCF for CHS and CFDST K-joints is similar.

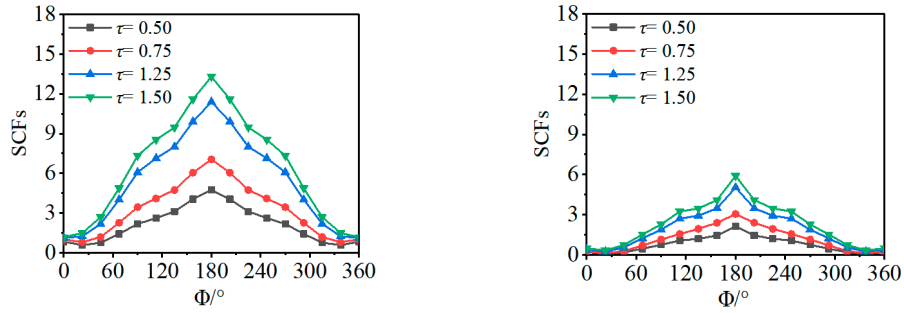

Figure 26. Distribution of the hot spot SCF of K-joints.

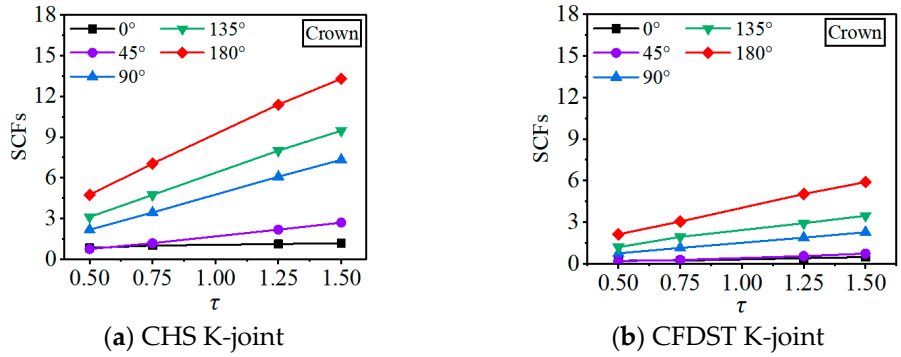

Figure 27. Magnitude of the hot spot SCF of K-joints.

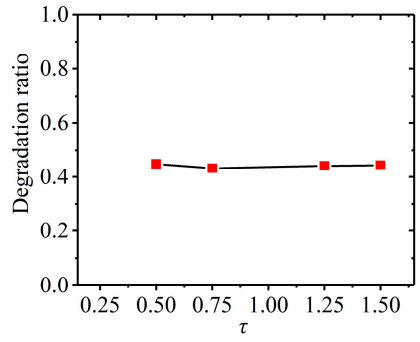

Figure 28. Degradation ratio of the hot spot SCF at different ratios τ.

5.6. Effect of Brace Angle θ

The hot spot SCF at the intersecting line weld of CHS and CFDST K-joints changing in the brace-to-chord angle θ is shown in Figure 29. The range of the hollow section ratio θ was 30 to 60°, and the rest of the variables β, γ, τ, and ζ remained constant, as shown in models K-FE-19 to K-FE-22 for CHS K-joints and K-FE-41 to K-FE-44 for CFDST K-joints in Table 9. The distribution trend of hot spot SCFs of CHS and CFDST K-joints is basically identical. The magnitude of the hot spot SCF at the positions of the crown heel, saddle, and

crown toe of the intersecting line is shown in Figure 30. The hot spot SCF clearly increases with the included angle θ increasing from 30 to 60°. However, when the included angle θ is less than 50°, the hot spot SCF remains stable. That is, the included angle θ has little influence on the hot spot SCF of CFDST K-joints when θ is smaller than 50°.

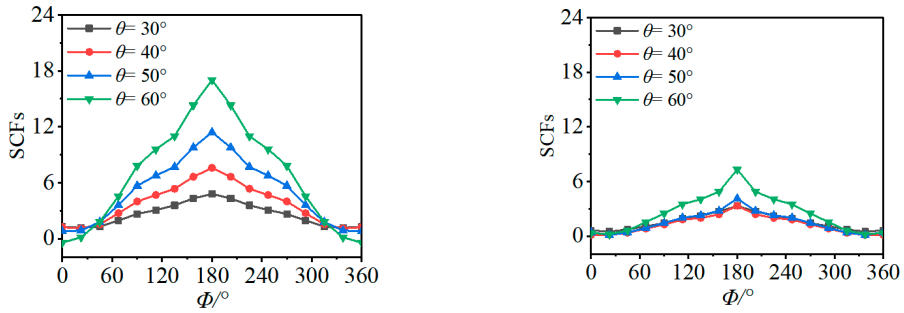

(**a**) CHS K-joint (**b**) CFDST K-joint

Figure 29. Distribution of the hot spot SCF of K-joints.

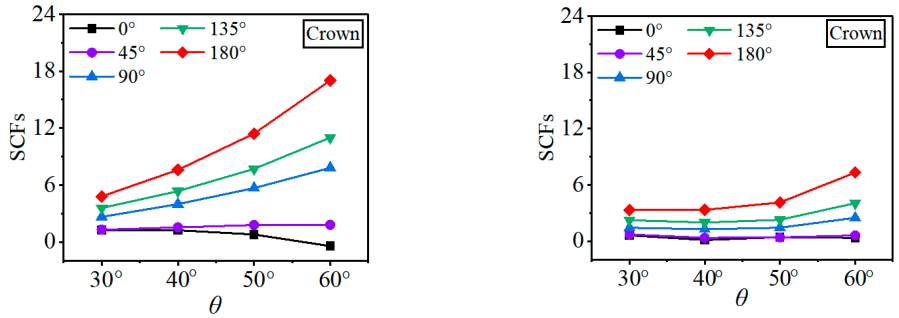

(**a**) CHS K-joint (**b**) CFDST K-joint

Figure 30. Magnitude of the hot spot SCF of K-joints.

Figure 31 shows the degradation ratio η of the maximum hot spot SCF of CFDST K-joints compared to CHS K-joints. Ratio η decreases and then increases with the angle θ. Ratio η decreased to the minimum of 0.35 when the angle θ was 50°. Therefore, for CFDST K-joints, it is suggested that the included angle θ between the brace and the chord may be about 50°.

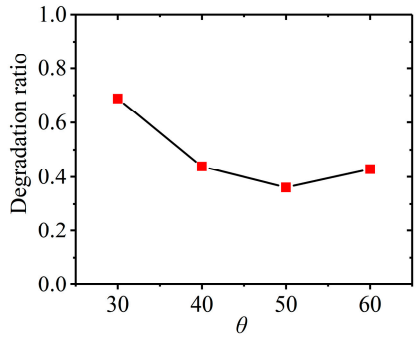

Figure 31. Degradation ratio of the hot spot SCF at different angles θ.

6. Proposed SCF Calculation Equations

6.1. Calculation Equations in Design Guidelines or Codes

Multiplication of nominal stress with the pertinent SCF enables the computation of the hot spot stress within tubular joints. However, accurately ascertaining SCFs at these critical points presents a significant hurdle. To address this, CIDECT-8 [18], DNV [19], API [39], and LR [40] provide rigorous algorithms for calculating the SCFs pertaining to K-joints.

(1) CIDECT-8 [18]

The present design guide offers refined mathematical expressions for determining the SCFs of CHS K-joints experiencing primary axial load balance:

Chord:

$$SCF_{\mathrm{ch,ax}} = \left[\frac{\gamma}{12}\right]^{0.4}\left[\frac{\tau}{0.5}\right]^{1.1} SCF_{\mathrm{o,ch,ax}} = \text{correction factor} \cdot SCF_{\mathrm{o,ch,ax}} \tag{17}$$

Brace:

$$SCF_{\mathrm{b,ax}} = \left[\frac{\gamma}{12}\right]^{0.5}\left[\frac{\tau}{0.5}\right]^{0.5} SCF_{\mathrm{o,b,ax}} = \text{correction factor} \cdot SCF_{\mathrm{o,b,ax}} \tag{18}$$

where $SCF_{\mathrm{o,ch,ax}}$ and $SCF_{\mathrm{o,b,ax}}$ are values when γ = 12 and τ = 0.5, and are calculated according to the corresponding requirements of CIDECT-8. When γ and τ are other values, a correction factor is used for the calculation.

The validity ranges for the SCF equations are as follows:

$0.30 \le \beta \le 0.60$

$12 \le \gamma \le 30$

$0.25 \le \tau \le 1.00$

$30^\circ \le \theta \le 60^\circ$

(2) API [39]

The API code provides the SCF calculation formula (Efthymiou equation) for CHS K-joints under the axial load applied by the chord.

Chord:

$$\begin{aligned} SCF_{\mathrm{c}} = {} & \tau^{0.9}\gamma^{0.5}(0.67 - \beta^2 + 1.16\beta)\sin\theta\left(\frac{\sin\theta\mathrm{max}}{\sin\theta\mathrm{min}}\right)^{0.30}\left(\frac{\beta\mathrm{max}}{\beta\mathrm{min}}\right)^{0.30} \\ & \times\left[1.64 + 0.29\beta^{-0.38}\arctan(8\xi)\right] \end{aligned} \tag{19}$$

Brace:

$$\begin{aligned} SCF_{\mathrm{b}} = {} & 1 + (1.97 - 1.57\beta^{0.25})\tau^{-0.14}(\sin\theta)^{0.7} SCF_{\mathrm{c}} + \sin 1.8(\theta_{\max} + \theta_{\min}) \\ & (0.131 - 0.084\arctan[14\xi + 4.2\beta] \cdot C\beta^{0.5}\tau^{-1.22} \end{aligned} \tag{20}$$

where the parameter ξ is defined as the ratio of the distance between the weld toes of the two braces g to the outer diameter of the chord. For gap joints, the coefficient C = 0.

The validity ranges for the SCF equations are as follows:

$0.20 \le \beta \le 1.00$

$8 \le \gamma \le 32$

$0.20 \le \tau \le 1.00$

$20^\circ \le \theta \le 90^\circ$

Moreover, the API code provides a consideration of the effect of full grouting of the chord on joint behavior, by replacing the thickness of the chord with an equivalent effective thickness T_{eff}:

$$T_{\mathrm{eff}} = 0.035D + 0.93T \tag{21}$$

(3) DNV [19]

DNV offers the same formulas to those provided by the API for calculating the SCFs of CHS K-joints. In addition, it prescribes an equivalent effective thickness T_{e} for cases where the chord is fully grouted. Furthermore, DNV introduces an additional amendment to account for the influence of grout-filled joints between annular members, as expressed below:

$$T_{\mathrm{e}} = T + 0.45T_1 \tag{22}$$

where T_1 is inner tube thickness.

(4) LR [40]

Smedley and Fisher [40] critically evaluated several classical equations for Stress Concentration Factor (SCF) parameters and, based on the strengths and weaknesses inherent in these equations, they derived the LR parameter equation as follows:

$$T1 = \tau\gamma^{1.2}\beta(2.12 - 2\beta)\sin^2\theta \tag{23}$$

$$T2 = \tau\gamma^{0.2}(3.5 - 2.4\beta)\sin^{0.3}\theta \tag{24}$$

$$T3 = 1 + \tau^{0.6}\gamma^{1.3}\beta(0.76 - 0.7\beta)\sin^{2.2}\theta \tag{25}$$

$$T4 = 2.6\beta^{0.65}\gamma^{(0.3-0.5\beta)} \tag{26}$$

$$SCF_{CS} = 1.22 \times (T1_A S1_{AB} - T1_B S1_{BA} IF1_{AB}) \times (F1_A \; or \; F2_A) \tag{27}$$

$$SCF_{CC} = 1.25 \times (T2_A S2_{AB} - T2_B S2_{BA} IF2_{AB}) + B0_A \times B1_A \tag{28}$$

$$SCF_{BS} = 1.12 \times (T3_A S1_{AB} - T3_B S1_{BA} IF3_{AB}) \times (F1_A \; or \; F2_A) \tag{29}$$

$$SCF_{BC} = 1.26 \times (T4_A S2_{AB} - T4_B S2_{BA} IF4_{AB}) \tag{30}$$

where SCF_{CS}, SCF_{CC}, SCF_{BS}, and SCF_{BC}, respectively, denote the SCFs at the saddle (90°) and crown (180°) for both the chord and brace; T represents T-joint coefficient capturing geometrical influences; S embodies the strengthening effect contributed by the additional brace; IF stands for the influence factor applicable to tubular K-joints; F is the short tube correction factor; and B approximates the stress in the chord for a simple specimen configuration.

The S coefficient in the above equations can be calculated as follows:

$$S1_{ij} = \left[1 - 0.4\exp(-30x_{ij}^2(\frac{\beta_i}{\beta_j})^2(\frac{\sin\theta_i}{\gamma}))\right] \tag{31}$$

$$S2_{ij} = \left[1 + \exp(-2x_{ij}^2(\frac{1}{\gamma^{0.5}\sin^2\theta_j}))\right] \tag{32}$$

$$x_{ij} = 1 + (g_{ij}\sin\theta_i/\beta_i) \tag{33}$$

where g_{ij} is the gap between brace i and brace j.

The IF coefficient can be calculated as follows:

$$IF1_{ij} = \beta_i(2.13 - 2\beta_i)\gamma^{0.2}\sin\theta_i(\frac{\sin\theta_i}{\sin\theta_j})^P\exp(-0.3x_{ij}) \tag{34}$$

$$IF2_{ij} = \left[20 - 8(\beta_i + 1)^2\right]\exp(-3x_{ij}) \tag{35}$$

$$IF3_{ij} = \beta_i(2.0 - 1.8\beta_i)\gamma^{0.2}(\frac{\beta_{min}}{\beta_{max}})(\frac{\sin\theta_i}{\sin\theta_j})^P\exp(-0.5x_{ij}) \tag{36}$$

$$IF4_{ij} = (-1.5\beta_i)\exp(-x_{ij}) \tag{37}$$

where p should be satisfied when $\theta_i > \theta_j$, $p = 1$; When $\theta_i < \theta_j$, $p = 5$.

The F coefficient can be calculated as follows:

$$F1 = \begin{cases} 1.0 & \alpha \geq 12 \\ 1 - (0.83\beta - 0.56\beta^2 - 0.02)\gamma^{0.23}\exp(-0.21\gamma^{(-1.16)}\alpha^{2.5}) & \alpha < 12 \end{cases} \tag{38}$$

$$F2 = \begin{cases} 1.0 & \alpha \geq 12 \\ 1 - (1.43\beta - 0.97\beta^2 - 0.03)\gamma^{0.04}\exp(-0.71\gamma^{(-1.38)}\alpha^{2.5}) & \alpha < 12 \end{cases} \tag{39}$$

The B coefficient can be calculated as follows:

$$B0 = \begin{cases} 0.00 \\ \frac{C\tau(\beta - \tau/(2\gamma))(\alpha/2 - \beta/\sin\theta)\sin\theta}{(1 - 3/(2\gamma))} \end{cases} \tag{40}$$

$$B1 = 1.05 + \frac{30\tau^{1.5}(1.2-\beta)(\cos^4\theta + 0.15)}{\gamma} \quad (41)$$

where C denotes the end restraint parameter for the chord. When the ends of the chord are fully fixed, C equals 0.5; conversely, if the ends are hinged, C is taken as 1.0. Conventionally, in structural analyses, C is often assumed to be 0.7. The applicability scope of this formula extends to:

$0.13 \leq \beta \leq 1.00$
$10.0 \leq \gamma \leq 35.0$
$0.25 \leq \tau \leq 1.00$
$30^\circ \leq \theta \leq 90^\circ$
$0.00 \leq g \leq 1.00$

In addition, for tube joints with β = 1, corrections need to be made at the saddle:

$$\beta = 1 - (\frac{\tau}{\gamma}\sin^{0.65}(\psi^\circ)) \quad (42)$$

In the above context, the variable ψ° signifies the extent of weld shrinkage, with a commonly prescribed default value of 20°.

These highlighted SCF equations hold a distinguished status as seminal formulations extensively employed and referenced by a multitude of researchers across the field. They have served as the bedrock upon which subsequent, more accurate equations have been developed. Despite these advancements, these initial formulas continue to hold substantial relevance and practical worth today. This study further explores and validates the efficacy of these foundational expressions.

6.2. Proposed Equations

Utilizing the hot spot stress approach and pertinent attributes inherent to CHS and CFDST K-joint configurations (parameters β, γ, τ, θ, and ζ), a suite of 360 numerical models comprising CHS and CFDST K-joints has been systematically generated to appraise SCFs. By employing multivariate, non-linear regression techniques and harnessing the outcomes from conducted finite element calculations, commensurate equations for the estimation of SCFs have been derived. Within the framework of parameter examination, it should be noted that, under axial loading conditions, peak stress concentrations customarily materialize at the weld interfaces of the chord. Henceforth, two tailored formulas have been derived to compute the maximal SCF along the weld toes of the chord, as detailed subsequently:

$$SCF_{\max} = (1.262 + 0.228\beta - 0.280\tau - 3.178\theta)\times (2.446 - 0.360\gamma^{0.709} - 2.112\tau) \quad R^2 = 0.955 \quad (43)$$

$$SCF_{\max} = (1.830 - 14.419\beta - 13.922\tau + 9.911\theta + 2.604\xi + 0.572\beta\gamma + 9.486\beta\tau + 29.427\tau^2\theta - 0.243\gamma\xi) \times (-1.193 + 1.298\gamma^{0.041} - 0.111\tau) \quad R^2 = 0.915 \quad (44)$$

where R^2 is the correlation coefficient.

6.3. Verifications

Figure 32 illustrates a systematic comparison between the computed outcomes derived from the developed parametric equations and those resulting from meticulous numerical analyses. The results confirm the robustness of the proffered formulations in accurately predicting the SCFs of CFDST K-joints. The study confines the parameter space to the range of geometrically relevant dimensions stipulated by DNV [19] for tubular joints in offshore structures, and extends to encompass ζ to examine its effects on SCFs. The precise parameter intervals investigated are delineated as follows:

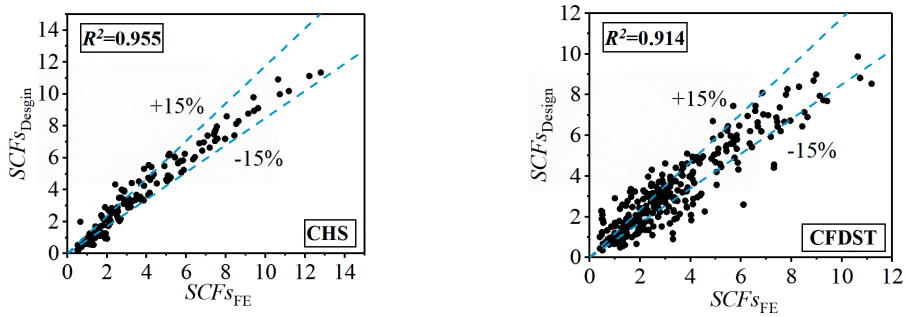

(**a**) CHS K-joint (**b**) CFDST K-joint

Figure 32. Comparison of SCF results calculated by a parametric equation and finite element method.

$0.4 \leq \beta \leq 0.8$
$10 \leq \gamma \leq 30$
$0.4 \leq \tau \leq 1.5$
$30^\circ \leq \theta \leq 60^\circ$
$0 \leq \zeta \leq 0.915$

The UK Department of Energy (DoE) [41] has recommended the following assessment criteria. Within these criteria, P/R denotes the ratio of predicted to measured values.

(1) For a given dataset, if [P/R < 1.0] is not exceeding 25% and [P/R < 0.8] does not exceed 5%, the parameter equation is deemed reasonable. Similarly, when [P/R > 1.5] exceeds 50%, the computed outcome from the parameter equation is generally considered conservative.

(2) If the condition satisfies 25% < [P/R < 1.0] ≤ 30% and/or 5% < [P/R < 0.8] ≤ 7.5%, the parameter equation is categorized as marginally acceptable and requires further scrutiny.

(3) For all other circumstances, the proposed formula is judged to have lower precision and fails to meet the required standards.

Acknowledging the prevalent tendency of underestimation in parameter fitting equations, the strict need to consider instances where P/R was less than unity was relaxed in the evaluation process [42]. In compliance with preceding guidelines and adhering to the DoE's established standards, Equations (43) and (44) underwent assessment as illustrated in Table 10. To align with these criteria, a corrective coefficient was integrated into Equation (45) as demonstrated below:

$$D_{\max} = SCF_{\max(\text{Design})} / SCF_{\max} \tag{45}$$

where $SCF_{\max}$ is determined by the provided equation, and the value of $SCF_{\max(\text{Design})}$ should conform to the aforementioned criteria.

Table 10. Evaluation results of the parametric equations.

No.	Evaluation Criteria				Conclusion		Correction Factor
	P/R < 0.8		P/R > 1.5				
	Previous	Subsequent	Previous	Subsequent	Previous	Subsequent	
Equation (43)	13.9% > 5%	3.6% < 5%	2.2% < 50%	12.4% < 50%	Needs Correction	Satisfy	1.216
Equation (44)	16.5% > 5%	4.8% < 5%	9.6% < 50%	23.2% < 50%	Needs Correction	Satisfy	1.283

Through a comprehensive comparative analysis, the optimal value for the correction factors was computed, as expressed in Equations (46) and (47):

$$SCF_{\max(\text{Desgine})} = 1.256 SCF_{\max} \tag{46}$$

$$SCF_{\max(\text{Design})} = 1.283 SCF_{\max} \quad (47)$$

Conforming to the criteria established by the (DoE), an appraisal of the modified equation was undertaken, and the ensuing results subsequent to this adjustment are displayed in Table 10.

Both the test data in this study and obtained from previous studies [23,43] were adopted for validation. Meanwhile, the SCF values calculated using the Efthymiou equation, the LR equation [40], and the specifications from both the API [39] and DNV [19] were compared with Equations (46) and (47). Tables 11 and 12 comprehensively present the geometric parameters of the tubular joints and their corresponding computational outcomes. Specifically, SCF_{eq} denotes the results obtained from Equations (45) and (46), while SCF_{Test} represents the experimental or literature-derived data. Observations reveal that both the novel equations proposed herein and the equations advocated by prevailing industry standards effectively approximate the SCFs within CHS K-joints. Nevertheless, the application of equivalent thickness methodologies in API and DNV specifications to estimate the SCFs in CFDST K-joints leads to computationally derived results that lean towards overestimation. Conversely, the equations introduced in this research offer predictions that demonstrate a closer congruence with actual measured data. It is noteworthy that the Efthymiou equation and the LR equation are specifically utilized for the calculation of CHS K-joints. Meanwhile, the API employs Equation (21) and the DNV uses Equation (22) to calculate the equivalent thickness, which is subsequently applied in the computation of SCFs for CFDST K-joints.

Table 11. Geometric parameters of the joints.

Specimen No.	Name of the Specimen in the Literature	Type	Literature	D	α	β	γ	τ	θ	ζ
S1	OC300-6-IC0-0-BR168-8-1	K	This study	300	12	0.56	25.00	1.33	45	
S2	OC300-6-IC0-0-BR168-8-2	K	This study	300	12	0.56	25.00	1.33	45	
S3	OC300-6-IC203-8-BR121-8	K	This study	300	12	0.40	25.00	1.33	45	0.715
S4	OC300-10-IC203-8-BR102-14	K	This study	300	12	0.34	15.00	1.40	45	0.725
S5	OC300-5-IC180-5-BR121-8	K	This study	300	12	0.40	30.00	1.60	45	0.621
S6	K1-13	K	Tong et al. [36]	219	16.27	0.58	13.32	0.76	45	
S7	K2-23	K		219	16.27	0.58	18.25	0.75	45	
S8	K3-23	K		219	16.27	0.58	13.69	1.01	45	
S9	K4-23	K		219	16.27	0.41	18.25	0.75	45	
S10		K	Eq. Efthymiou [19,39]	600	15.00	0.60	15.00	0.60	30	
S11		K		600	15.00	0.40	20.00	0.60	45	
S12		K		600	15.00	0.80	15.00	0.60	45	
S13		K	Eq. LR [40]	600	15.00	0.60	25.00	0.40	45	
S14		K		600	15.00	0.80	20.00	0.80	45	
S15		K		600	15.00	0.60	15.00	0.60	60	
S16		K	API [39], DNV [19]	300	15.00	0.40	18.75	1.00	45	1.000
S17		K		300	15.00	0.60	18.75	1.00	45	1.000
S18		K		300	15.00	0.40	15.00	1.00	45	1.000
S19		K		300	15.00	0.40	10.71	1.00	45	1.000

Table 12. Comparison of the calculated results of SCF_{eq} with specifications and test results.

Specimen No.	SCF_{eq}	$SCF_{Efthymiou}$	SCF_{LR}	SCF_{API}	SCF_{DNV}	SCF_{Test}
S1	7.23	6.83	10.49			8.47
S2	7.23	6.83	10.49			9.00
S3	6.65			2.43	5.17	10.47
S4	5.21			1.79	3.11	5.62
S5	8.48			2.64	7.62	13.39
S6	2.52	3.00	3.57			4.96
S7	3.49	3.47	4.39			4.14
S8	3.73	3.93	4.79			5.83
S9	3.59	3.48	4.63			4.57
S10	3.15	2.57	2.52			
S11	3.26	2.97	4.07			
S12	2.11	2.39	2.55			
S13	3.16	2.30	3.10			
S14	3.90	3.58	4.43			
S15	3.63	2.57	3.75			
S16	3.90			2.08		
S17	4.13			2.07		
S18	3.58			2.22		
S19	3.11			2.36		

7. Conclusions

Experimental and numerical investigations on the hot spot stress of CHS and CFDST K-joints were performed. The test results were assessed to discern the hot spot stress characteristics of CHS and CFDST joints based on SCFs. Subsequently, a refined finite element model was developed considering the fillet welds between the brace and chord, and the model was validated against the experimental results. Based on the developed FE models, parametric analyses were conducted to assess the influence of geometry on SCFs. Based on both experimental and numerical studies, the SCF calculation formula for CHS and CFDST joints was proposed. The findings can be summarized as follows:

(1) Joints with identical geometric dimensions exhibited fundamentally similar patterns in stress concentration factor distribution. However, the presence of infill concrete could significantly reduce the SCFs of K-joints, when comparing the values between CHS and CFDST joints.

(2) The rate of maximum SCF reduction exhibited sensitivity to the ratio of radius to thickness of the chord γ and brace angle θ, particularly with respect to hollow section ratio ζ. An increase in γ would lead to a decrease in the maximum SCF reduction rate.

(3) The hollow section ratio ζ had a relatively minor influence on the distribution pattern of SCFs. As ζ decreased, the inner layer of the infill concrete and tube could significantly improve the radius stiffness of the chord, thereby reducing cross-sectional deformation and alleviating stress concentration phenomena in the joint region. When ζ declined to a certain threshold, the stiffness of the CFDST might approach that of a fully concrete-filled steel tube. The rate of reduction varied minimally when ζ lay between 0.317 and 0.704.

(4) Through the regression analysis, a formula was derived to calculate the maximum hot spot stress concentration factor for CHS and CFDST joints, which demonstrated high precision and reliability.

Research is primarily focused on fatigue life assessment under axial loading conditions, which may not fully encapsulate the complex loading scenarios encountered in engineering

applications. Furthermore, the finite element models utilized in this analysis are simplified representations of actual joints and may not account for all possible variations in material properties and manufacturing processes. Despite these limitations, this study offers valuable insights into the behavior of CFDST K-joints and contributes to the existing body of knowledge in the field.

Author Contributions: Conceptualization, Q.X.; data curation, L.M.; formal analysis, G.L. and C.H.; methodology, Q.X.; project administration, L.M.; supervision, F.X.; validation, Z.L.; writing—original draft, L.Z.; writing—review & editing, F.X. All authors have read and agreed to the published version of the manuscript.

Funding: This work was financially sponsored by the Natural Science Foundation of Chongqing (CSTB2023NSCQ-MSX0576), China Power Engineering Consulting Group Corporation Limited research program "Research on Key Technologies for Compact and Lightweight Offshore Wind Power Transmission Converter Stations" (Project No: DG2-A06-2022) and the Fundamental Research Funds for the Central Universities (2022CDJQY-009).

Data Availability Statement: The original contributions presented in the study are included in the article, further inquiries can be directed to the corresponding author.

Acknowledgments: The authors would like to sincerely acknowledge the support from the Natural Science Foundation of Chongqing (CSTB2023NSCQ-MSX0576) and the Fundamental Research Funds for the Central Universities (2022CDJQY-009).

Conflicts of Interest: Authors Qian Xia and Chao Hu were employed by the company Central Southern China Electric Power Design Institute Co., Ltd. Authors Ling Ma, Gang Li and Zhenhai Liu were employed by the company China Power Engineering Consulting Group Co., Ltd. and Ocean Energy Engineering Technology Research Institute of CPECC. The remaining authors declare that the research was conducted in the absence of any commercial or financial relationships that could be construed as a potential conflict of interest. The authors declare that this study received funding from China Power Engineering Consulting Group Corporation Limited. The funder was not involved in the study design, collection, analysis, interpretation of data, the writing of this article or the decision to submit it for publication.

References

1. Dong, F.; Shi, L.; Ding, X.; Li, Y.; Shi, Y. Study on China's renewable energy policy reform and improved design of renewable portfolio standard. *Energies* **2019**, *12*, 2147. [CrossRef]
2. Oh, K.-Y.; Nam, W.; Ryu, M.S.; Kim, J.-Y.; Epureanu, B.I. A review of foundations of offshore wind energy convertors: Current status and future perspectives. *Renew. Sustain. Energy Rev.* **2018**, *88*, 16–36. [CrossRef]
3. Akadiri, P.O.; Chinyio, E.A.; Olomolaiye, P.O. Design of a sustainable building: A conceptual framework for implementing sustainability in the building sector. *Buildings* **2012**, *2*, 126–152. [CrossRef]
4. Tetiranont, S.; Sadakorn, W.; Rugkhapan, N.T.; Prasittisopin, L. Enhancing sustainable railway station design in tropical climates: Insights from Thailand's architectural theses and case studies. *Buildings* **2024**, *14*, 829. [CrossRef]
5. Danatzko, J.M.; Sezen, H. Sustainable structural design methodologies. *Pract. Period. Struct. Des. Constr.* **2011**, *16*, 186–190. [CrossRef]
6. Zain, M.; Ngamkhanong, C.; Kang, T.H.K.; Usman, M.; Prasittisopin, L. Modal-based fragility analysis of high-rise tubular structures: A methodology for vulnerability assessment. *Structures* **2024**, *63*, 106289. [CrossRef]
7. Shi, W.; Park, H.; Chung, C.; Baek, J.; Kim, Y.; Kim, C. Load analysis and comparison of different jacket foundations. *Renew. Energy* **2013**, *54*, 201–210. [CrossRef]
8. Tian, W.; Wang, Y.; Shi, W.; Michailides, C.; Wan, L.; Chen, M. Numerical study of hydrodynamic responses for a combined concept of semisubmersible wind turbine and different layouts of a wave energy converter. *Ocean. Eng.* **2023**, 272. [CrossRef]
9. Ricciardelli, F.; Maienza, C.; Vardaroglu, M.; Avossa, A.M. Wind energy into the future: The challenge of deep-water wind farms. *Wind. Struct.* **2021**, *32*, 321–340.
10. Li, J.; Guo, Y.; Lian, J.; Wang, H. Mechanisms, assessments, countermeasures, and prospects for offshore wind turbine foundation scour research. *Ocean. Eng.* **2023**, *281*, 114893. [CrossRef]
11. Ouyang, C.; Luo, J.; Wang, T.; Zhang, P. Research on the effect of burial depth on the bearing characteristics of three helical piles jacket foundation for offshore wind turbines. *J. Mar. Sci. Eng.* **2023**, *11*, 1703. [CrossRef]
12. Song, S.-S.; Chen, J.; Xu, F. Mechanical behaviour and design of concrete-filled K and KK CHS connections. *J. Constr. Steel Res.* **2022**, *188*, 107000. [CrossRef]

13. Xu, G.; Tong, L.; Zhao, X.-L.; Zhou, H.; Xu, F. Numerical analysis and formulae for SCF reduction coefficients of CFRP-strengthened CHS gap K-joints. *Eng. Struct.* **2020**, *210*, 110369. [CrossRef]
14. Ferrotto, M.F.; Fenu, L.; Xue, J.-Q.; Briseghella, B.; Chen, B.-C.; Cavaleri, L. Simplified equivalent finite element modelling of concrete-filled steel tubular K-joints with and without studs. *Eng. Struct.* **2022**, *266*, 114634. [CrossRef]
15. Wang, K.; Tong, L.-W.; Zhu, J.; Zhao, X.-L.; Mashiri, F.R. Fatigue behavior of welded T-joints with a CHS brace and CFCHS chord under axial loading in the brace. *J. Bridge Eng.* **2013**, *18*, 142–152. [CrossRef]
16. Xu, F.; Chen, J.; Jin, W.-L. Experimental investigation of SCF distribution for thin-walled concrete-filled CHS joints under axial tension loading. *Thin-Walled Struct.* **2015**, *93*, 149–157. [CrossRef]
17. Zhao, X.-L. *Fatigue Design Procedure for Welded Hollow Section Joints*; Abington Publishing: Lisbon, TN, USA, 1999.
18. Zhao, X.-L.; Herion, S.; Ja, P. *Design Guide for Circular and Rectangular Hollow Section Joints under Fatigue Loading*; CIDECT Publication: TUV-Verlag, Germany, 2000.
19. *DNV-RP-C203 2011*; Det Norske Veritas. Fatigue Design of Offshore Steel Structures. p. 176. Available online: https://www.dnv.com/oilgas/download/dnv-rp-c203-fatigue-design-of-offshore-steel-structures/ (accessed on 6 May 2024).
20. Xiao, L.; Wei, X.; Zhao, J.; Wu, C. Hot spot stress concentration factor of CFST T/Y joints based on modified equivalent thickness. *Structure* **2023**, *51*, 910–925. [CrossRef]
21. Zheng, J.; Nakamura, S.; Ge, Y.; Chen, K.; Wu, Q. Formulation of stress concentration factors for concrete-filled steel tubular (CFST) T-joints under axial force in the brace. *Eng. Struct.* **2018**, *170*, 103–117. [CrossRef]
22. Zheng, J.; Nakamura, S.; Okumatsu, T.; Nishikawa, T. Formulation of stress concentration factors for concrete-filled steel tubular (CFST) K-joints under three loading conditions without shear forces. *Eng. Struct.* **2019**, *190*, 90–100. [CrossRef]
23. Tong, L.; Xu, G.; Zhao, X.-L.; Zhou, H.; Xu, F. Experimental and theoretical studies on reducing hot spot stress on CHS gap K-joints with CFRP strengthening. *Eng. Struct.* **2019**, *201*, 109827. [CrossRef]
24. *JGJ 81-2002, J*; Technical Specification for Welding of Steel Structure of Building. China Standards Press: Beijing, China, 2002.
25. *ISO-6892-1*; Metallic Materials—Tensile Testing—Part 1: Method of Test at Room Temperature. ISO: Geneva, Switzerland, 2019.
26. Huang, Y.; Young, B. The art of coupon tests. *J. Constr. Steel Res.* **2014**, *96*, 159–175. [CrossRef]
27. *GB/T50081*; Standard for Test Methods of Concrete Physical and Mechanical Properties. China Architecture & Building Press: Beijing, China, 2019.
28. Shao, Y.B. Geometrical effect on the stress distribution along weld toe for tubular T- and K-joints under axial loading. *J. Constr. Steel Res.* **2007**, *63*, 1351–1360. [CrossRef]
29. Shao, Y.B.; Lie, S.-T. Experimental and numerical studies of the stress concentration factor (SCF) of tubular K-joints. *Eng. Mech.* **2006**, *23*, 79–85.
30. Van Wingerde, A.M.; Packer, J.A.; Wardenier, J. Criteria for the fatigue assessment of hollow structural section connections. *J. Constr. Steel Res.* **1995**, *35*, 71–115. [CrossRef]
31. *D1.1—Structural Welding Code-Steel*; American Welding Society: Miami, FL, USA, 2004; p. 634.
32. Shen, J.C. Fatigue Performance of CFDST Members under Bending. Master's Thesis, Tsinghua University, Beijing, China, 2022.
33. Hai, H.L. *Concrete-Filled Steel Tubular Structures: Theory and Practice*, 3rd ed.; Science Press: Beijing, China, 2016.
34. Xu, F. Mechanical Behaviour of Concrete-Filled Thin-Walled Steel Tube Members and Connections. Ph.D. Thesis, Zhejiang University, Hangzhou, China, 2016.
35. Mohamed, H.; Zhang, L.; Shao, Y.; Yang, X.; Shaheen, M.; Suleiman, M. Stress concentration factors of CFRP-reinforced tubular K-joints via zero point structural stress approach. *Mar. Struct.* **2022**, *84*, 103239. [CrossRef]
36. Tong, L.W.; Xu, G.W.; Yang, D.L.; Mashiri, F.R.; Zhao, X.L. Fatigue behavior and design of welded tubular T-joints with CHS brace and concrete-filled chord. *Thin-Walled Struct.* **2017**, *120*, 180–190. [CrossRef]
37. Li, W.; Cheng, Y.-F.; Wang, D.; Han, L.-H.; Zhao, X.-L. Behaviour of high-strength CFDST chord to CHS brace T-joint: Experiment. *Eng. Struct. 2020 219*, 110780. [CrossRef]
38. Tong, L.; Xu, G.; Zhao, X.-L.; Yan, Y. Fatigue tests and design of CFRP-strengthened CHS gap K-joints. *Thin-Walled Struct.* **2021**, *163*, 107694. [CrossRef]
39. *Recommended Practice for Planning, Desigining and Constructing Fixed Offshore Plaforms*; American Petroleum Institute: Washington, DC, USA, 1993; p. 274.
40. Smedley, P.; Fisher, P. Stress concentration factors for simple tubular joints. In Proceedings of the ISOPE International Ocean and Polar Engineering Conference, Edinburgh, UK, 11–16 August 1991.
41. *Background Notes to the Fatigue Guidance of Offshore Tubular Joints*; United Kingdom Department of Energy: London, UK, 1983; p. 123.
42. Bomel Consulting Engineers. *Assessment of SCF Equations Using Shell/KSEPL Finite Element Data*. C5970R0201 REV C. 1994. Available online: http://refhub.elsevier.com/S0951-8339(22)00078-8/sref52 (accessed on 6 May 2024).
43. Qiu, C.F. Study on Hot Spot Stress of Concrete-Filled Tubular T-Joints and Y-Joints. Master's Thesis, Xihua University, Chengdu, China, 2021.